First Comet Observations with NIRSPEC-2 at Keck: Outgassing Sources of Parent Volatiles and Abundances Based on Alternative Taxonomic Compositional Baselines in 46P/Wirtanen

Boncho P Bonev, Neil Dello Russo, Michael A Disanti, Emily C Martin, Gregory Doppmann, Ronald J Vervack, Geronimo L Villanueva, Hideyo Kawakita, Erika L Gibb, Michael R Combi, et al.

The Planetary Science Journal, 2:45 (17pp), 2021 April https://doi.org/10.3847/PSJ/abd03c

First Comet Observations with NIRSPEC-2 at Keck: Outgassing Sources of Parent Volatiles and Abundances Based on Alternative Taxonomic Compositional Baselines in 46P/Wirtanen

Boncho P. Bonev[1], Neil Dello Russo[2], Michael A. DiSanti[3,4], Emily C. Martin[5], Gregory Doppmann[6], Ronald J. Vervack, Jr.[2], Geronimo L. Villanueva[3,4], Hideyo Kawakita[7], Erika L. Gibb[8], Michael R. Combi[9], Nathan X. Roth[10,11], Mohammad Saki[8], Adam J. McKay[1,3], Martin A. Cordiner[4,11,12], Dennis Bodewits[13], Jacques Crovisier[14], Nicolas Biver[14], Anita L. Cochran[15], Yinsi Shou[9], Younas Khan[8], and Kumar Venkataramani[13]
[1] Department of Physics, American University, Washington, DC 20016, USA; bonev@american.edu
[2] Space Department, Johns Hopkins University Applied Physics Laboratory, Laurel, MD 20723, USA
[3] Solar System Exploration Division, Planetary Systems Laboratory, MS 693, NASA Goddard Space Flight Center, Greenbelt, MD 20771, USA
[4] Goddard Center for Astrobiology, NASA Goddard Space Flight Center, Greenbelt, MD 20771, USA
[5] Department of Astronomy & Astrophysics, University of California Santa Cruz, Santa Cruz, CA 95064, USA
[6] W. M. Keck Observatory, Kamuela, HI 96743, USA
[7] Koyama Astronomical Observatory, Kyoto Sangyo University, Motoyama, Kamigamo, Kita-ku, Kyoto 603-8555, Japan
[8] Department of Physics and Astronomy, University of Missouri–St. Louis, Saint Louis, MO 63121, USA
[9] Department of Climate and Space Sciences and Engineering, University of Michigan, Ann Arbor, MI 48109, USA
[10] Universities Space Research Association, Columbia, MD 21046, USA
[11] Solar System Exploration Division, Astrochemistry Laboratory Code 691, NASA Goddard Space Flight Center, Greenbelt, MD, 20771 USA
[12] Department of Physics, Catholic University of America, Washington, DC 20064, USA
[13] Physics Department, Auburn University, Auburn, AL 36832, USA
[14] LESIA, Observatoire de Paris, Université PSL, CNRS, Sorbonne Université, Université de Paris, 5 place Jules Janssen, F-92195 Meudon, France
[15] McDonald Observatory, University of Texas at Austin, Austin, TX 78712, USA
Received 2020 August 5; revised 2020 November 20; accepted 2020 November 23; published 2021 March 9

Abstract

A major upgrade to the NIRSPEC instrument at the Keck II telescope was successfully completed in time for near-infrared spectroscopic observations of comet 46P/Wirtanen during its exceptionally close flyby of Earth in 2018 December. These studies determined the abundances of several volatiles, including C_2H_2, C_2H_6, CH_3OH, NH_3, HCN, H_2CO, and H_2O. Long-slit spatial distributions of gas rotational temperature and column density are diagnostic for the presence of icy grains in the coma and understanding if different volatiles are associated with common or distinct outgassing sources. These spatial distributions suggest that C_2H_2, C_2H_6, and HCN have a common outgassing source, whereas H_2O and CH_3OH have additional, more extended sources. The synergy of these findings with observations by space missions (Rosetta and EPOXI) motivates continuing studies to address whether or not C_2H_6, C_2H_2, and HCN have a common source of release (plausibly associated with CO_2) in a larger sample of comets and whether systematic differences exist in the release of these species compared to H_2O and CH_3OH. Abundances of volatiles are reported relative to H_2O, as traditionally done, as well as C_2H_6. While not unique, the choice of C_2H_6 demonstrates the value of extending the chemical taxonomy of parent volatiles in comets toward additional compositional "baselines" and, importantly, closer integration between coma abundances and the underlying volatile associations as revealed by spatial distributions. Our findings on composition and sources of outgassing include information relevant to future evaluations of 46P/Wirtanen as a prospective spacecraft target.

Unified Astronomy Thesaurus concepts: Solar system (1528); Small solar system bodies (1469); Comets (280); Short period comets (1452); Comae (271)

1. Introduction

This paper reports high-resolution ($\lambda/\Delta\lambda \sim 25{,}000$) near-infrared (near-IR) spectroscopic observations of comet 46P/Wirtanen conducted during this comet's long-anticipated close flyby to Earth in mid-December of 2018. As part of a worldwide observing campaign, these were the first observations of a comet with the recently upgraded NIRSPEC spectrograph on the Keck II telescope (Martin et al. 2016, 2018). Focused on parent (or primary; originally stored as ices in comet nuclei) volatiles, this work addresses four main questions, motivated by both fundamental science and the need to better characterize 46P/Wirtanen as a prospective spacecraft mission target.

1. Do parent volatiles have common or distinct outgassing sources, which may point to volatile associations (or lack thereof) among particular species in the ices of the nucleus of 46P/Wirtanen?
2. What causes the perceived "hyperactivity" of 46P/Wirtanen? Such hyperactivity has been hypothesized based on previous observations, revealing higher water production rates than commonly observed from similarly small (<1 km) comet nuclei (Groussin & Lamy 2003).
3. How do the abundances of species measured in 46P/Wirtanen compare to those of other comets?
4. Can these abundance measurements serve as a basis for extension of the current compositional taxonomy for parent volatiles?

These questions are not unique to 46P/Wirtanen but have been of great interest in understanding cometary activity (sources and mechanisms of outgassing; questions 1 and 2) and composition (questions 3 and 4). The main motivation of these studies is to understand better the role of comets as relics from the protosolar nebula. Cometary composition provides a crucial link to the chemistry of the protoplanetary disk midplane and the ice inventory in its very central opaque parts, where many comets likely formed (A'Hearn et al. 2012; Willacy et al. 2015; Drozdovskaya et al. 2016; Eistrup et al. 2019; Kamp 2020). The recently completed Rosetta mission to comet 67P/Churyumov–Gerasimenko (CG) reinforced this view. While it revealed significant spatial, seasonal, and short-term temporal changes in comet outgassing patterns, it also confirmed that 67P/CG has retained a rich inventory of ices with a degree of devolatilization which is lower than that of inner solar system objects, thereby strengthening the view of comets as among the most pristine objects in our solar system (Rubin et al. 2019).

Intensified sublimation of ices upon approach to the Sun is considered a primary driver of cometary activity, giving rise to a coma (exosphere) and the ion and dust tails. However, decoding the in-depth mechanism(s) of "how do comets work?" (A'Hearn 2017) is still a priority in post-Rosetta cometary science, vitally important for disentangling the effects of natal (pertaining to solar system origins) versus various postformative processes on present-day comet composition. Spacecraft missions and remote-sensing studies play complementary and equally significant roles in this process.

Missions provide unprecedented detail on the nature of comets (see Keller & Kührt 2020). For example, the last two comets visited by spacecraft showed different outgassing behavior. Rosetta primarily observed sublimation directly from ices in the nucleus of 67P/CG (Biver et al. 2019), while EPOXI revealed that H_2O vaporized mainly from icy grains ejected in the coma of 103P/Hartley 2 (A'Hearn et al. 2011; Fougere et al. 2013; Protopapa et al. 2014).

Because missions are necessarily restricted to only a few accessible targets, astronomical remote sensing is indispensable for understanding comets as a population, which includes objects with a wide range of dynamical histories, physical appearances, nucleus sizes and shapes, rotational properties, gas productivity ranges, and inner coma compositional abundances. A major result from ground-based observational databases is that the measured relative abundances of parent and product (radicals produced in the coma) species vary substantially among the sample of comets studied so far (A'Hearn et al. 1995; Crovisier et al. 2009; Fink 2009; Schleicher & Bair 2014; Cochran et al. 2015; Dello Russo et al. 2016; Roth et al. 2020 and references therein).

Parent volatiles have been studied (albeit in vastly different levels of detail) in about 30 near-isotropic comets (dynamically linked to the Oort Cloud) and about 15 ecliptic comets (dynamically linked to the scattered Kuiper disk). The latter group is dominated by Jupiter-family comets (JFCs) like 46P/Wirtanen that have traditionally been underrepresented in studies of all parent species, giving additional motivation for our observations.

The following sections describe in sequence the historically favorable apparition of 46P/Wirtanen (Section 2), our Keck observations for which the upgrade of NIRSPEC was completed (Section 3), and the specific measurements addressing each aforementioned science question (Section 4), followed by a discussion (Section 5) and summary (Section 6).

2. The Historically Favorable Apparition of 46P/Wirtanen in 2018

Comet 46P/Wirtanen has been a proposed spacecraft target several times and was the original Rosetta target before a delayed launch (Keller & Kührt 2020). Being both highly active and one of the easiest comets to reach by spacecraft, it remains a plausible future mission target. The 2018 apparition of this comet was especially timely, coming on the heels of the Rosetta mission and as the new generation of near-IR spectrographs (iSHELL at the NASA Infrared Telescope Facility, IRTF; see DiSanti et al. 2017; NIRSPEC-2 at Keck, this paper) plus advances in millimeter/submillimeter capabilities (Atacama Large Millimeter/submillimeter Array, ALMA; Cordiner et al. 2014, 2017) were being successfully utilized for comet science. During the period of its maximum gas productivity (near perihelion; 2018 December), 46P/Wirtanen passed within ~30 lunar distances (0.077 au), remaining within 0.1 au from Earth for 20 consecutive days with outstanding observing geometry. These factors together are very rare and resulted in one of the best apparitions for any JFC in modern history. The combination of (near) naked-eye brightness and very small geocentric distance (Δ) is not expected for either 46P or other comparatively bright JFCs in the near future, further signifying the importance of the late 2018–early 2019 observational opportunity.

Therefore, 46P/Wirtanen was a top-priority target in a worldwide observing campaign (http://wirtanen.astro.umd.edu/) involving both amateur and professional astronomers. Our near-IR observations at Keck were coordinated with several investigations targeting parent or product species, including (but not limited to) the extensive IRTF campaign (2018 December–2019 February; Dello Russo et al. 2019; Faggi et al. 2019a; Saki et al. 2020) and the high spatial resolution ALMA mapping measurements in early 2018 December (Cordiner et al. 2019; see Section 5.1 for synergistic results).

3. A Major Upgrade to the NIRSPEC Instrument

3.1. Observations

These were the first comet observations with the NIRSPEC-2 spectrograph. NIRSPEC at Keck II (McLean et al. 1998) has enabled a number of comet studies in the last two decades. In 2018, the W. M. Keck Observatory completed a major upgrade to this instrument (Martin et al. 2016, 2018), with the challenging goal to have it "on sky" specifically in time for the 46P/Wirtanen flyby of Earth in December. The NIRSPEC upgrade replaced the 1024 × 1024 pixel Aladdin III detector with a 2048 × 2048 pixel HAWAII-2RG detector, significantly improving the readout electronics and sensitivity, and increasing the spectral coverage of a given instrument setting. A truly remarkable effort by the NIRSPEC team was required to complete the upgrade on time; the spectrograph was tested on sky in engineering runs (on UT 2018 December 9, 14, and 15) immediately prior to the scheduled science observations (on UT December 17 and 18).

We note that no significant outbursts have been reported close in time to our observations (Moulane et al. 2019; Kelley et al. 2021; Farnham et al. 2021). Farnham et al. and Kelley et al. independently identified an outburst event on UT December 12, ~5 days prior to our first observing date (UT December 17).

Table 1 shows a condensed observing log. The comet was observed shortly after its UT December 16 (2018) closest approach to Earth. The optimal work plan required one

Table 1
Observing Log and H_2O Production Rates

UT Date (2018)	R_h[a] (au)	Δ[a] (au)	$d\Delta/dt$[a] km s^{-1}	T_{int}[b,c] (minutes)	Slit PA[c] Range	Sun–Comet PA	Phase Angle	NIRSPEC Setting	$Q(H_2O)$[d] (10^{25} s^{-1})
Dec 17.4	1.057	0.078	0.8	3 16	~252° 144°–97°	91°	19°	KL2	749 ± 34
Dec 18.4	1.058	0.078	1.6	10	131°–110°	102°	18°	KL1	903 ± 30

Notes.
[a] Here, R_h, Δ, and $d\Delta/dt$ are, respectively, the heliocentric distance, geocentric distance, and topocentric line-of-sight velocity of 46P/Wirtanen.
[b] Here, T_{int} is the total integration time on source.
[c] Observations were limited to rotator stationary mode, in which the PA of the slit changes with time. For UT December 17, data taken pretransit (slit PA ~ 252°; T_{int} = 3 minutes) and posttransit (slit PA = 144°–97°, T_{int} = 16 minutes) were coadded in order to achieve the maximum signal-to-noise ratio in the weakest emissions. We then verified that our spatial distributions along the slit (Sections 4.1, 4.2) are dominated entirely by the posttransit data. See further discussion in the main text.
[d] Water production rate, as described in Section 4.3.

echelle/cross-disperser setting per night. On UT December 17, we utilized an instrument setting (KL2; echelle/cross-disperser angle = 62.°10/33.°10, covering eight noncontiguous *L*-band orders 20–27) optimized to sample the maximum number of species, including C_2H_2 (acetylene), C_2H_6 (ethane), HCN (hydrogen cyanide), NH_3 (ammonia), H_2CO (formaldehyde), and H_2O. On UT December 18, we used a complementary setting (KL1; echelle/cross-disperser angle = 64.°20/33.°10) that encompasses many of the brightest emissions of H_2O, CH_3OH (methanol), and C_2H_6 because these were more easily detectable even under the suboptimal atmospheric conditions on that date. We note that the Doppler shift was near zero during our observations; hence, the lines of CH_4 encompassed in our settings were completely obscured by their counterpart absorptions in the terrestrial atmosphere.

Long-slit spectra were obtained using a standard A–B–B–A sequence of telescope nodding, with both the A and B beams in the slit, positioned symmetrically with respect to its midpoint and spatially separated by 12″ (half the slit length). For NIRSPEC-2, this nodding sequence was initially tested during our observations, and systematic corrections to the nod direction were obtained, ensuring the target remained well centered in both the A and B beams. Additional details on the methodology for data acquisition, reduction, and spectral analysis are presented in multiple sources (e.g., Bonev 2005, see pp. 263–267 for spatial registration of individual frames; Bonev et al. 2006; Villanueva et al. 2011a; DiSanti et al. 2018; Dello Russo et al. 2020). Because the observed IR emissions are optically thin, comparison between modeled and measured spectra (Section 3.2) allows for determining spatial distributions along the slit (Section 4.1), gas rotational temperatures (Section 4.2; based on the relative intensities between optically thin IR lines), production rates (Section 4.3), and relative abundances (Section 4.4).

Table 1 also lists the phase angles (~18°) and the ranges in slit position angle (PA) covered on each observing date (Note c). Importantly, only the rotator stationary mode for NIRSPEC was functional for our long-slit observations, meaning that the PA of the slit varied over the course of our observations. Furthermore, observers did not have control of the initial slit PA value. These constraints did not affect our comparisons of spatial distributions (Section 4.1) among volatiles because each such comparison only includes molecules sampled simultaneously within the same spectrograph setting. This capability eliminates any effects of short-term variability (when spatial profiles are compared) due to either changing PA or time variations in outgassing patterns associated with nucleus rotation. Furthermore, our spatial distributions on UT December 17 are heavily dominated by data spanning a ~50° range in PA, while on UT December 18, they entirely comprise data covering only a ~20° range in PA. On each date, the temporal coverage comprises only ~10% of the estimated rotation period of the comet (~9 hr; Jehin et al. 2018; Farnham et al. 2021).

3.2. Spectral Gallery

Figures 1–5 show molecular detections in 46P/Wirtanen throughout the *L* band (~2.8 to ~3.6 μm). A slit width of 0.″432 enabled a resolving power of $\lambda/\Delta\lambda \approx 25{,}000$. A measured spectrum is shown at the top of Figures 1, 2, 3, 4(a), and 5. Each spectrum consists of two components: (1) a strong near-IR dust continuum and (2) molecular emission in excess of the continuum. A best-fit continuum model (pink) accounts for the wavelength-dependent telluric extinction and is overlaid against the measured spectrum. The fully resolved atmospheric transmittance function was tightly constrained from both comet and contemporaneous standard star data using the Planetary Spectrum Generator (https://psg.gsfc.nasa.gov/; Villanueva et al. 2018).

The H_2O "hot-band" emissions near 2.85 μm are very prominent above the continuum (Figure 1) and were the easiest IR lines to discern in single A–B difference frames as displayed immediately following readout. The gas-to-continuum emission ratio was significantly lower at longer wavelengths (Figures 2–5); hence, in these cases, we also show on a separate scale (*y*-axis) the "residual" spectrum after subtraction of the (strong) modeled continuum, clearly revealing many molecular lines.

Molecular emission models are color-coded and shown below the measured spectrum in each figure to help identify IR lines of a particular species. Some emission models are further scaled vertically (e.g., $C_2H_2 \times 2$; Figure 4(a)) to better emphasize weaker emissions. Each emission model is based on previously tested and published emission efficiencies (*g* factors (photons s^{-1} mol^{-1}); see Bonev et al. 2006; DiSanti et al. 2006; Radeva et al. 2011; Villanueva et al. 2011b, 2012a, 2012b and references therein).

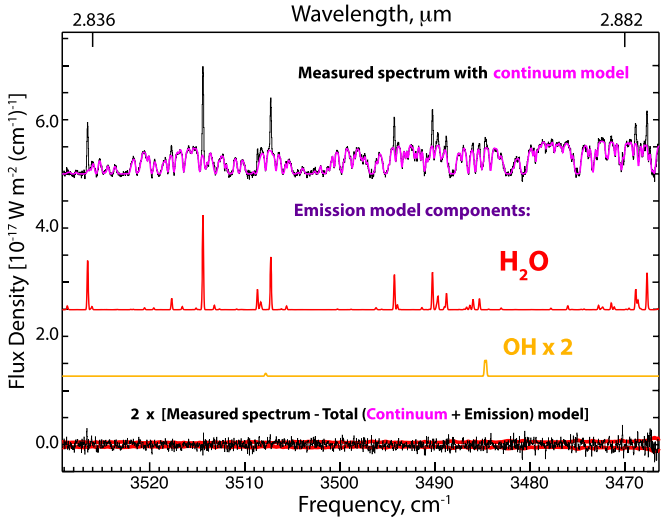

Figure 1. Spectrum of H_2O in comet 46P/Wirtanen (echelle order 27, KL1 setting; see Table 1 and Section 3). Several strong nonresonant fluorescence ("hot-band") lines of water are clearly seen above the continuum. These were the easiest IR emissions to discern in simple A–B difference frames as displayed immediately following readout during our observations. The spectrum consists of two components: a near-IR continuum and molecular emission in excess of the continuum. A best-fit continuum model (in pink) is overlaid against the measured spectrum. Molecular emission models are color-coded and shown below the measured spectrum. The photon noise ($\pm 1\sigma$) envelope is indicated by red lines in the "measured spectrum—total model" plot (bottom of the figure). A similar presentation for continuum and emission models is used in Figures 2–5.

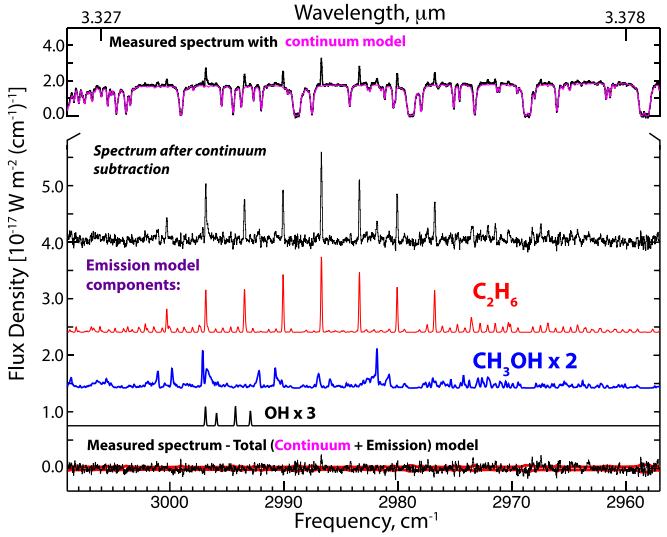

Figure 2. Spectrum (order 23, KL1) of C_2H_6 and CH_3OH. The "residual" spectrum after subtraction of the (strong) modeled continuum is shown on an expanded scale (y-axis) to better emphasize molecular emission lines (same for Figures 3–5). All spectral peaks in the C_2H_6 emission model (red) belong to the ν_7 vibrational band of this species. The emissions in the CH_3OH model (blue) belong to the ν_2 vibrational band.

Although the spectra in Figures 1 and 2 correspond to only 10 minutes of on-source integration time,[16] they are of very high quality, mainly due to the improved sensitivity of the HAWAII-2RG detector of NIRSPEC-2. We point out the very

[16] Most of this observing date (December 18) was "weathered out." Conditions improved at the end of the allocated half-night, when optimized nonsidereal tracking and systematic corrections to the nod pattern allowed quick accumulation of high-quality data.

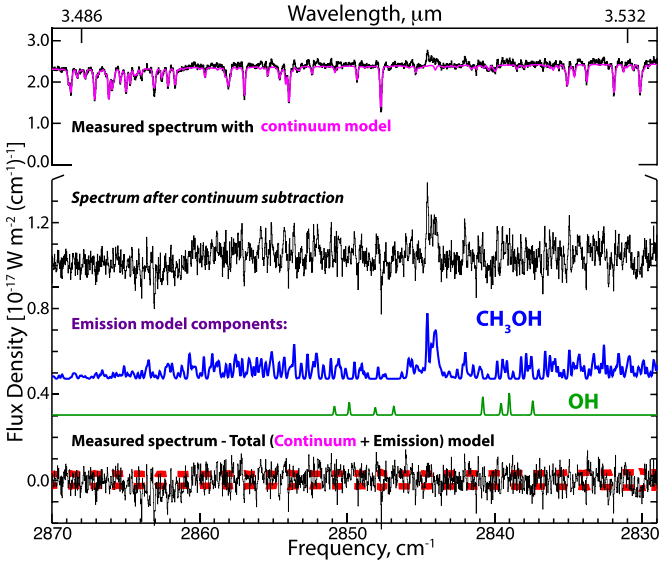

Figure 3. Spectrum of CH_3OH, showing nearly the entire ν_3 band (symmetric C–H stretch; order 22, KL1). The Q branch is the strong feature centered near 2844 cm^{-1} (3.516 μm), with R- and P-branch emissions shown to the left and right of this, respectively.

significant improvement in readout electronics, eliminating the so-called "row-chop" patterns that previously were time-variable and introduced a considerable source of "instrumental noise" (affecting detection limits) associated with the old NIRSPEC detector.

Figure 2 shows emissions from C_2H_6 (ν_7 band) and CH_3OH (ν_2 band). Figure 3 shows the brightest CH_3OH emissions (ν_3 band). Figure 4(a) shows one of the most spectrally "crowded" regions in the L band near 3 μm, with IR lines from HCN, H_2O, OH, C_2H_2, and NH_3. Because the continuum-subtracted spectrum is dominated by HCN, Figures 4(b)–(d) zoom into portions of this spectrum to better emphasize molecular detections, including weaker but clearly visible emission lines of C_2H_2 and NH_3. The detections of C_2H_2 and NH_3 are confirmed by summing the flux over all expected line positions for each species (after removing the spectral contributions of other volatiles), as described in Villanueva et al. (2009). Note that for NIRSPEC-2, the spectral range per echelle order is increased by roughly 30%, allowing sampling of acetylene (C_2H_2) emissions that have often been excluded in previous studies (Figure 4(d)).

Figure 5 shows the spectral region near ~3.41–3.47 μm, which was particularly challenging yet feasible to address. This spectrum presented the only means of obtaining the C_2H_6 production rate on UT December 17 because the frequency range covered on this date was optimized to include several other species (HCN, C_2H_2, and NH_3; see the description of the KL2 setting at the beginning of Section 3.1), thereby excluding the coverage of the strong ν_7 band of ethane measured on December 18 (Figure 2; KL1 setting).

The much weaker ν_5 band of C_2H_6 sampled here includes lines that are barely visible above the strong continuum (top panel of Figure 5). Furthermore, the spectrum includes CH_3OH emissions that were first studied quantitatively in the Halley-type comet 109P/Swift–Tuttle (DiSanti et al. 1995) and cataloged in spectral surveys of comets C/1999 H1 (Lee) and 103P/Hartley 2 based on comparison with laboratory data (Dello Russo et al. 2006, 2013). These IR emissions are also

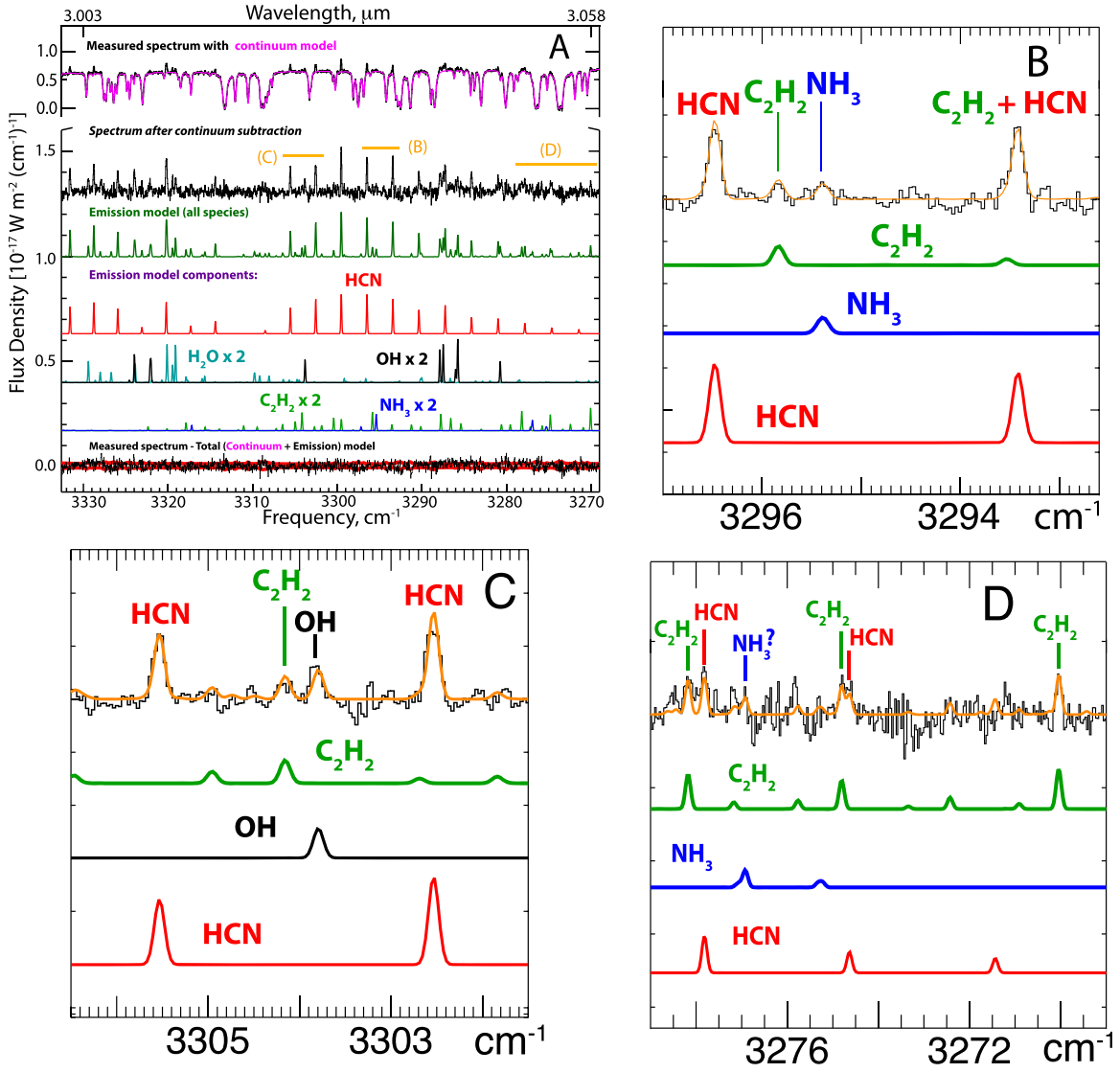

Figure 4. The spectrally "crowded" region near 3 μm (order 25, KL2), containing IR lines from several species, which can be identified via comparison with the models shown. (a) The continuum-subtracted spectrum is dominated by HCN (red model). The spectral ranges corresponding to panels (b)–(d) are marked with horizontal bars (orange). (b)–(d) Portions of this spectrum emphasize molecular detections of weaker but clearly visible emission lines of C_2H_2 and NH_3. The overall model of molecular emission (orange) is shown against the measured spectrum. The best spectral models of C_2H_2 (green), NH_3 (blue), and HCN (red) are shown below the measured spectrum.

prominent in 46P/Wirtanen, as shown in Figure 5, but are not included in current fluorescence models owing to the lack of line identifications. To address this challenge, we excluded all C_2H_6 lines blended with CH_3OH from quantitative analysis using the spectral survey of Hartley 2 as a guide. We also excluded regions of low and highly variable atmospheric transmittance, where continuum baseline uncertainties might be significant (Bonev et al. 2014). This left a sufficient number of C_2H_6 emissions (marked with red vertical lines in Figure 5) for analysis. In support of this approach, the resulting gas rotational temperature derived from the C_2H_6 ν_5 band (92 ± 6 K) is in excellent agreement with independent retrievals from both HCN (94^{+4}_{-3} K) and H_2O (89 ± 2 K) measured simultaneously (Section 4, Table 2), as predicted by thermodynamic models (see Section 4.2) and confirmed by many observations of the inner (collisional) coma in previously studied comets.

4. Results

4.1. A Test for Common or Distinct Outgassing Sources between Water and Other Volatiles

This section compares spatial distributions (profiles) of column density for the molecules with sufficiently bright IR emissions detected in 46P/Wirtanen: H_2O, C_2H_6, CH_3OH, HCN, and C_2H_2. Spatial profiles of simultaneously sampled water and other volatiles can test whether these species are associated with common or distinct outgassing sources. In particular, (1) volatiles sublimating from ices within the same source region(s) (nucleus, icy grains in the coma, or a combination of both) are expected to project into similar gas spatial profiles, and (2) major differences in spatial distributions point to entirely distinct outgassing sources or one or more additional outgassing source(s) for some volatiles.

The value of ground-based observations as a probe for heterogeneous outgassing has been demonstrated for several

Table 2
Molecular Production Rates and Abundances in 46P/Wirtanen from Keck/NIRSPEC-2

UT Date (2018)	Mol.	T_{rot}[a] (K)	Q_{nc}[b] (10^{25} s^{-1})	GF[b]	Q[b] (10^{25} s^{-1})	Relative Abundance[c]	
						(H_2O = 100)	(C_2H_6 = 1)
Dec 17	H_2O	89 ± 2	296 ± 7	2.53 ± 0.10	749 ± 34	100	131 ± 10
Dec 17	C_2H_6	92 ± 6	3.43 ± 0.15	1.66 ± 0.06	5.70 ± 0.32	0.76 ± 0.06	1.00
Dec 17	C_2H_2	(89)	0.34 ± 0.04	1.64 ± 0.21	0.55 ± 0.10	0.074 ± 0.013	0.097 ± 0.018
Dec 17	HCN	94^{+4}_{-3}	0.87 ± 0.02	1.68 ± 0.07	1.47 ± 0.07	0.20 ± 0.01	0.26 ± 0.02
Dec 17	NH_3[d]	(89)	1.96 ± 0.31	(2.53 ± 0.10)	4.97 ± 0.80	$0.66^{+0.11}_{-0.29}$	$0.87^{+0.15}_{-0.39}$
Dec 17				(1.68 ± 0.07)	3.30 ± 0.53		
Dec 17	H_2CO[e]	(89)	<0.19	(2.53)	<0.48	<0.064	<0.084
Dec 18	H_2O	87 ± 1	349 ± 4	2.59 ± 0.08	903 ± 30	100	151 ± 7
Dec 18	C_2H_6	84^{+5}_{-4}	3.74 ± 0.07	1.60 ± 0.04	5.98 ± 0.19	0.66 ± 0.03	1.00
Dec 18	CH_3OH	(87)	11.88 ± 0.48	2.30 ± 0.13	27.32 ± 1.91	3.03 ± 0.23	4.57 ± 0.35

Notes.
[a] Gas rotational temperature for a nucleus-centered aperture of ∼24 km (slit width) × ∼65 km (along slit). The T_{rot} measured for different species are in good agreement on each observing date. Values in parentheses are assumed.
[b] Nucleus-centered production rate (Q_{nc}), growth factor (GF), and global production rate (Q = GF × Q_{nc}).
[c] Relative abundances are expressed as ratios of global production rates.
[d] The GF for NH_3 cannot be constrained. The global production rates are therefore calculated independently, assuming that NH_3 tracks H_2O (GF = 2.53 ± 0.10) and HCN (GF = 1.68 ± 0.07). We adopt the relative abundance obtained with GF(H_2O), but the lower error bar incorporates the difference between GF(H_2O) and GF(HCN).
[e] The upper limit of H_2CO accounts for both stochastic and continuum baseline uncertainty and conservatively assumes the largest GF value measured on this observing date.

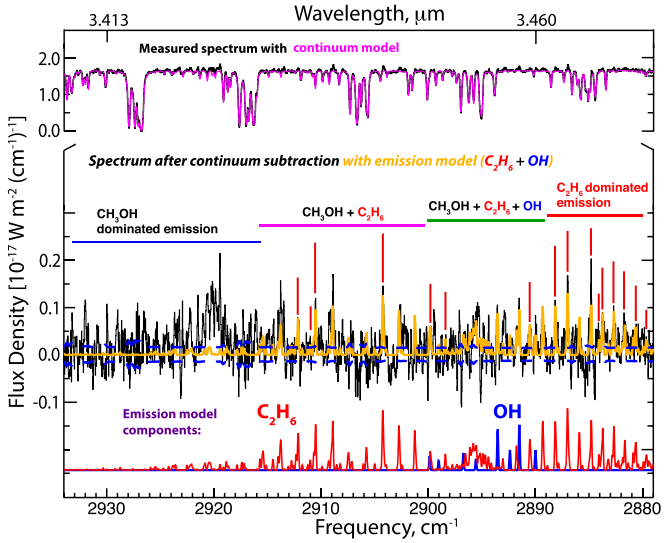

Figure 5. The spectral region ∼3.41–3.47 μm is dominated by the ν_5 band of C_2H_6 and by many lines of of CH_3OH (order 22, KL2). The residual spectrum following continuum subtraction is shown on a separate scale. The molecular model (C_2H_6 + OH; orange) is overlaid on this residual spectrum with the ($\pm 1\sigma$) photon noise envelope (blue dashed line). The C_2H_6 lines used for obtaining the production rate of ethane are marked with red vertical lines. Many CH_3OH lines were cataloged in spectral surveys of comets C/1999 H1 (Lee) and 103P/Hartley 2; these were based on a comparison with laboratory data. See the last paragraph of Section 3.2 for details.

comets (Villanueva et al. 2011a; DiSanti et al. 2014; Paganini et al. 2014a, 2014b and references therein), including EPOXI's target 103P/Hartley 2 (Dello Russo et al. 2011, 2013; Mumma et al. 2011; Bonev et al. 2013; Kawakita et al. 2013). We extended these studies to 46P/Wirtanen during its close approach to Earth, when the fine spatial scale (∼7 km pixel^{-1}) offered a transitional look between the very inner coma workings (revealed by space missions) and the more extended region of the collisional coma, typically sampled by ground-based IR studies.

Figure 6 shows the spatial distributions measured in 46P/Wirtanen. The panels are ordered by comeasured species, beginning with H_2O and C_2H_6, and then by overall data quality. The most accurate spatial profiles correspond to IR emission with a relatively high gas-to-continuum ratio, which minimizes continuum baseline uncertainties (Bonev et al. 2014) when isolating molecular emission. These include H_2O (Figures 6(a)–(e)); C_2H_6 (ν_7 band; Figure 6(a), December 18), HCN (Figure 6(c), December 17), and CH_3OH (Figure 6(d), December 18). Additional spatial distributions for C_2H_6 (ν_5 band; Figure 6(b), December 17) and CH_3OH (Figure 6(e), December 17) are also useful because they provide date-to-date comparison.

We also note that although in rotator stationary mode the slit PA varies (Table 1), on UT December 18, the x-axis (kilometers) on each spatial profile (Figures 6(a) and (c)) is fairly close to but not perfectly aligned with the "Sun–anti-Sun" projection on the sky plane (sunward is toward the "positive" distances). This orientation is significantly different from the physical Sun–anti-Sun direction at a phase angle of only ∼18°. Nevertheless, simultaneously measured spatial distributions provide meaningful information at any observing geometry.

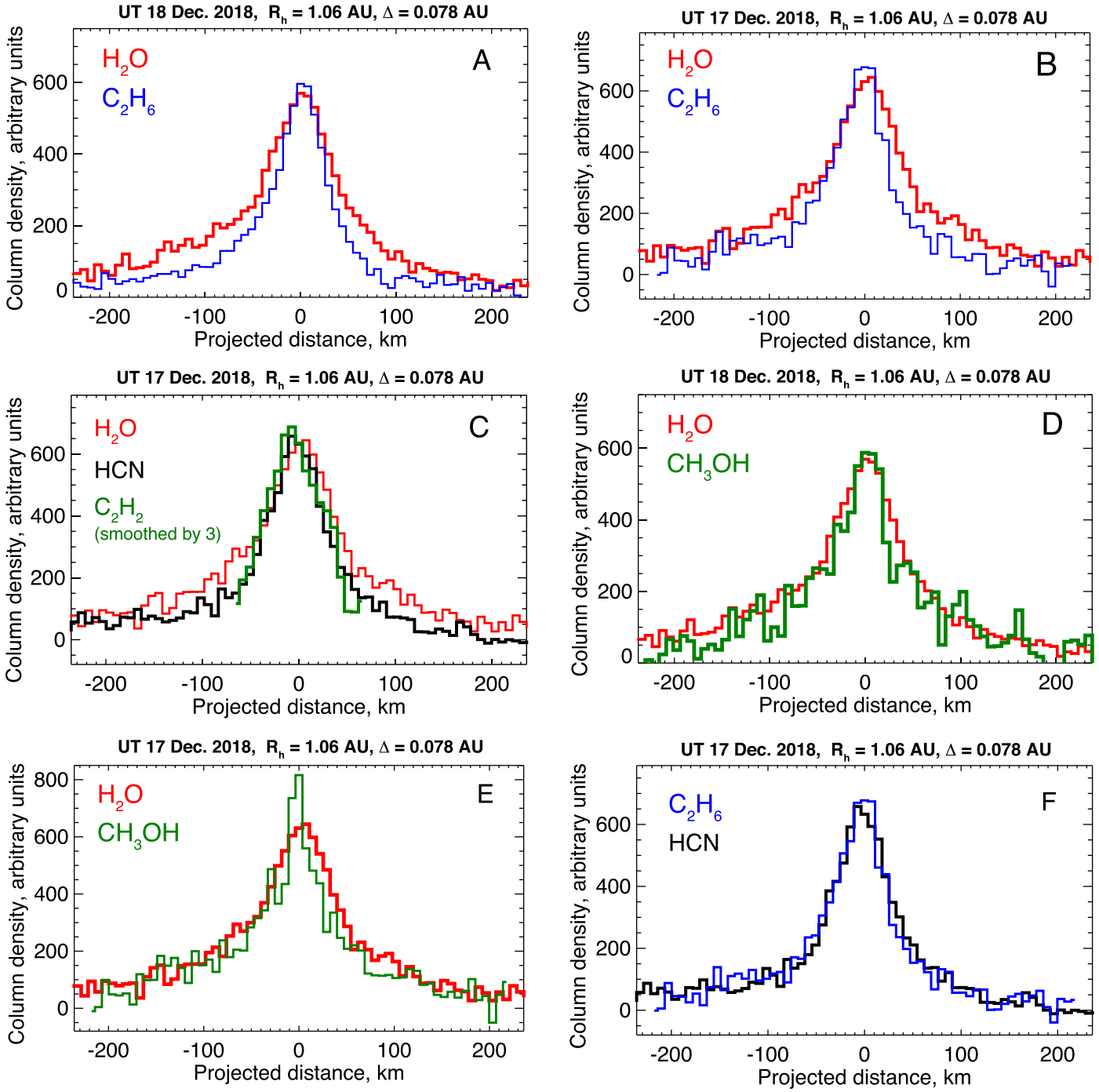

Figure 6. Spatial distributions for various volatiles with the observing date indicated on each plot. The distributions on each figure panel are measured simultaneously within the same spectrograph setting. Figure panels are ordered by comeasured species (i.e., beginning with H_2O vs. C_2H_6, our two primary compositional "baseline" molecules; see Section 4.4). (a) and (b) H_2O and C_2H_6. (c) H_2O, HCN, and C_2H_2 (smoothed by 3, as indicated). The extent of the C_2H_2 profile is limited by its weaker overall IR line brightness (see Figure 4). (d) and (e) H_2O and CH_3OH. (f) HCN and C_2H_6. All long-slit measurements were conducted in rotator stationary mode; therefore, the on-sky slit PA varied over the course of our observations (Table 1). On UT 2018 December 17, the slit PA = 252°–97° (as measured east of north); however, the spatial distribution is heavily dominated by measurements having a slit PA = 144°–97°. The Sun–comet line, as projected on the sky plane, is 91°, and the phase angle was 19°. On UT December 18, the slit PA varied between ∼131° and ∼110°, with the Sun–comet line projected at 102° at a phase angle of 18°. On this date, the projected sunward direction is thus nearly aligned with the positive *x*-axis.

As a consistency check, we verified that the continuum emissions comeasured at different wavelengths (different echelle orders within the same spectrograph setting) are very well aligned spatially. Representative continuum profiles (pink histogram) for each observing date are shown in Figures 7(a) and (b) in comparison with H_2O (red histogram). Differences in gas distributions (Figure 6) then suggest the following outgassing patterns in 46P/Wirtanen.

(1) H_2O reveals a more spatially extended release compared to C_2H_6, HCN, and C_2H_2. The water spatial profiles appear systematically broader than those of the three other species. The broader H_2O distributions are

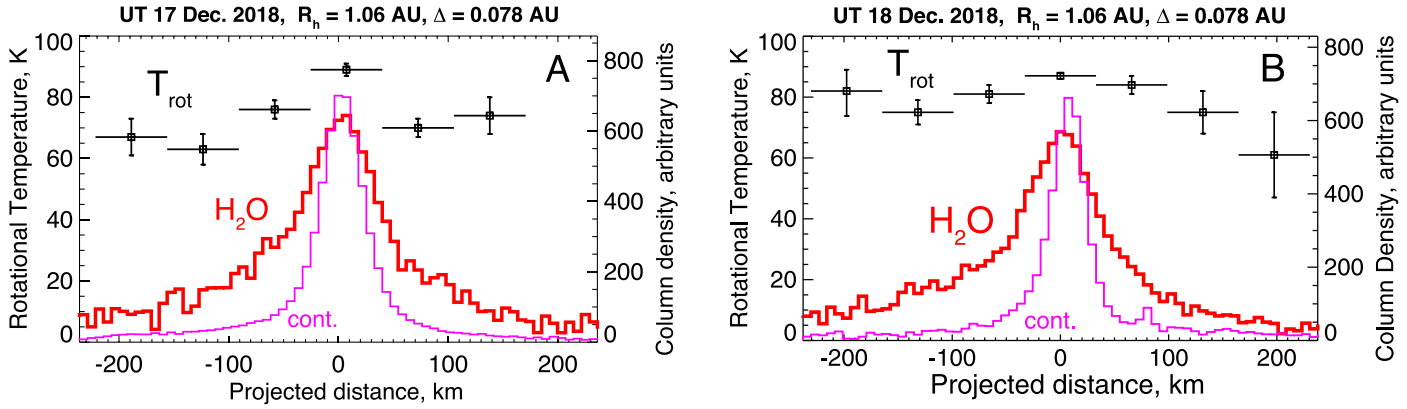

Figure 7. Spatial distribution of H_2O rotational temperature (black squares), H_2O column density (red histogram), and IR continuum near 2.9 μm (pink histogram) from our long-slit IR measurements of 46P/Wirtanen. See Table 1 and caption of Figure 6 for a description of slit orientation.

consistent with some water being released from icy grains in the inner coma.

(2) The spatial distributions of comeasured HCN, C_2H_2, and C_2H_6 closely track each other (see Figures 6(c) and (f)). This close spatial association implies that these species are connected with a common outgassing source and plausibly are connected as ices in the nucleus of 46P/Wirtanen. Figure 6(c) provides a rare constraint on the outgassing of C_2H_2; its relatively weak IR lines generally do not have a sufficient signal-to-noise ratio for ground-based spatial studies. A notable exception is 103P, where C_2H_6, HCN, and C_2H_2 were similarly connected (Dello Russo et al. 2011).

(3) The distributions of CH_3OH are narrower and better peaked in their central parts compared to the profiles of H_2O (Figures 6(d) and (e)). In contrast, CH_3OH tracks H_2O more closely than the other trace species in the "wings" of the spatial profiles (distances exceeding ~50–100 km on both sides of the peak intensity). Therefore, CH_3OH may also have an extended source in the inner coma, in addition to direct release from the nucleus.

(4) The peak of the H_2O profile is offset from those of simultaneously measured C_2H_6 (Figure 6(b)), HCN (Figure 6(c)), and CH_3OH (Figure 6(e)) on December 17. However, on December 18, all measured volatiles peak at the same position, which most likely reflects a varying projection of the gas sources along the slit. Note that our two observations are separated by ~2.65 rotational periods and sample significantly different phases of the comet's rotation, during which illumination changed significantly (see Farnham et al. 2021; Knight et al. 2021).

4.2. Mechanism of Water Release as a Test for Hyperactivity

Figures 7(a) and (b) show the spatial distributions of water gas rotational temperature (T_{rot}; black squares; left y-axis) in comparison with column density (red histogram; right y-axis) for UT December 17 and 18, respectively. The methodology for these measurements, including evaluations of uncertainties beyond photon noise, is detailed in Bonev et al. (2008, 2013, 2014), and Villanueva et al. (2011a). Gas rotational temperatures were measured for successive fields of view (FoVs) along the slit. Each FoV covers a footprint area of ~24 km (slit width) × ~65 km (along the slit, indicated by the horizontal bar through each measurement point). Each T_{rot} measurement then represents an effective temperature for the gas column encompassed by the corresponding FoV (see Fougere et al. 2012). The 1σ uncertainties in T_{rot} are shown.

The measured spatial distributions suggest only a slightly decreasing (Figure 7(a); December 17) or even nearly constant (Figure 7(b); December 18) T_{rot} with projected distance from the nucleus, in stark contrast to the large negative spatial gradient in H_2O gas column density. These measurements reflect the thermodynamic environment in the innermost coma, where collisions equilibrate the rotational temperature to the kinetic temperature of the gas (Combi et al. 2004). What mechanism then prevents the temperature from decreasing in a similar fashion as the more rapidly falling column density?

The T_{rot} profiles are indicative of the competition between cooling and heating processes in the collisional coma. The main cooling process is near-adiabatic expansion, which generally implies a more significant (up to several tens of kelvins) decrease in T_{rot}, assuming that water sublimates solely from the cometary nucleus. Under this assumption, Direct simulation Monte Carlo (DSMC) calculations for comet 67P/CG by Tenishev et al. (2008) and Marschall et al. (2019) are in fairly good agreement with radial temperature profiles from Rosetta/MIRO (Biver et al. 2019), which pertain to nucleocentric distances within ~20 km, where this parameter drops to ~45 K. That near-adiabatic expansion cooling results in larger negative gradients in T_{rot} (either radial or column-averaged) than measured in 46P/Wirtanen is a general feature of a large variety of coma thermodynamic models, independent of a particular observing geometry (Gombosi et al. 1986; Combi et al. 2004; Tenishev et al. 2008; Zakharov et al. 2008; Fougere et al. 2012, 2016; Fougere 2014; Shou et al. 2016 and references therein). Our measurements therefore suggest a heating source in the coma, which competes with the near-adiabatic cooling. We consider several possibilities.

The more extended spatial distribution of H_2O column density compared to other species and dust (Section 4.1) strongly suggests an icy grain source of H_2O gas in the inner coma. Fougere et al. (2012) and Fougere (2014) showed that both local and line-of-sight averaged temperatures are very sensitive to the presence or lack of such an extended source. In particular, significant coma heating can occur when a fraction of H_2O gas is not released directly from the nucleus but instead from icy grains or chunks sublimating in the coma. Water gas

then vaporizes from grains at initially "warm" temperatures, comparable to the sublimation temperature of H_2O (~180–200 K). This warm gas imparts energy through collisions to the cooler ambient cloud, thereby working against near-adiabatic expansion cooling.

Electron–H_2O collisions may also contribute to coma heating, even when sublimation from coma grains is absent (Cravens & Körösmezey 1986; Xie & Mumma 1992; Fougere et al. 2012). Depending on electron densities (which are uncertain), collisions with electrons may plausibly have nonnegligible effects on the observed temperatures. However, electron–H_2O collisions alone cannot explain the extended column density profiles of water (Fougere et al. 2012), supporting the role of an extended coma source of H_2O gas. Similarly, dust–gas collisions might have some effects on temperatures only.

Photochemical heating should also be considered. In this process, fast dissociation products are partially thermalized, thereby transferring energy to the coma gas. However, this process is predicted to have a far greater significance at much smaller heliocentric distances (R_h) than for 46P, where the solar UV fluxes are higher. At $R_h \approx 1$ au, photochemical heating is generally more evident at larger distances from the nucleus (>1000–10,000 km; Combi & Smyth 1988; Combi et al. 1999; Fougere 2014). We therefore conclude that the spatial distributions of both water column density and gas temperature are consistent with the presence of an extended source of icy grains whose sublimation leads to warming of the inner coma.

A significant icy grain coma was revealed by the Deep Impact spacecraft (EPOXI mission) during its flyby of 103P/Hartley 2 (A'Hearn et al. 2011; Protopapa et al. 2014), consistent with supporting ground-based T_{rot} measurements (Bonev et al. 2013). Comets 103P and 46P have often been referred to as "hyperactive," implying that they have higher H_2O production rates than most comets of similarly small (~1 km in mean diameter) size. EPOXI demonstrated that sublimating coma ice could be the root cause of elevated gas productivity, rather than uncommonly large active surface areas (Groussin & Lamy 2003) with pure nucleus sublimation. This is also a viable mechanism here, contributing to the observed activity levels in 46P/Wirtanen, though not necessarily with a similar ratio between nucleus and extended source contributions as seen in 103P.

Sublimation from icy grains dominated the total H_2O production of comet 73P-B/Schwassmann–Wachmann 3, as is evident by comparison between T_{rot} spatial profiles (Bonev et al. 2008) and DSMC thermodynamic models (Fougere et al. 2012). A similar analysis of the measurements from Figure 7 with a DSMC model has the potential to more precisely quantify the contributions of each water gas release mechanism (nucleus versus icy grain sources; in Section 4.3 of this paper, we provide an estimate), test the nature of subliming grains (for example, pure ice versus "dirty" ice; note added in proof: Protopapa et al. 2021, exclude pure icy grains as a possible extended source of H2O based on nondetection of water-ice absorption features in 46P/Wirtanen), and evaluate whether electron–H_2O and/or dust–gas collisions affect the observed temperatures. These analyses justify a separate future paper focused on addressing whether an extended icy grain source is merely nonnegligible or (similar to 73P-B and 103P; Fougere et al. 2013) the dominant source of H_2O gas.

The measurements presented here (Sections 4.1 and 4.2) can also serve as a test of any coma thermodynamic simulations that account for both nucleus and extended sources of volatiles, limited not only to water but also to species like C_2H_6 and HCN, whose spatial distributions (Figures 6(a) and (c)), while narrower than those of H_2O and CH_3OH, appear broader than those of the dust continuum (Figures 7(a) and (b)). This effect could also be due to the decoupling of gas and dust outflow within ~10 nucleus radii (~10 km) for comets with moderately high production rates (Tenishev et al. 2011).

4.3. Production Rates and Estimate of the Extended Water Source Contribution

The differences in spatial distributions discussed in the preceding sections are accounted for in our measured abundances in the inner coma of 46P/Wirtanen. Table 2 shows nucleus-centered production rates (Q_{nc}) and global production rates (Q) derived by the well-documented Q-curve method (see Xie & Mumma 1996; Dello Russo et al. 1998; DiSanti et al. 2001, 2016; Bonev et al. 2006, 2017; Villanueva et al. 2011a). This formalism provides the ratio Q/Q_{nc}, commonly referred to as the "growth factor" (GF). It accounts for slit losses in flux due to atmospheric seeing; hence, invariably, GF > 1. Such slit losses are identical for all species sampled within a given spectrograph setting. Importantly, differences in GFs among simultaneously measured volatiles then reflect differences in their spatial distributions; the larger GFs for H_2O and CH_3OH indicate that their spatial profiles appear significantly broader (Figure 6) than those of HCN, C_2H_6, and C_2H_2, accounting for the possibility of both nucleus and extended sources of gas.

The GF measurements lead to global production rates ($Q = \mathrm{GF} \times Q_{nc}$) and can therefore provide an approximation for estimating the contribution of extended icy grain sources of H_2O release. The product $Q(H_2O) = \mathrm{GF}(H_2O) \times Q_{nc}(H_2O)$ represents the total water production rate (~749 and $\sim 903 \times 10^{25}$ s^{-1} for December 17 and 18, respectively; Table 2), including contributions from both nucleus and extended sources of gas. On the other hand, consider each part in the product $\mathrm{GF}(C_2H_6) \times Q_{nc}(H_2O)$ (~490 and $\sim 560 \times 10^{25}$ s^{-1} for December 17 and 18, respectively).

We assume that the GFs of C_2H_6 and HCN are representative of the nucleus outgassing of all studied volatiles (including water) in 46P. In support of this assumption, on UT December 17, when these species were comeasured, their GFs have typical values for ground-based studies and agree within the errors, $\mathrm{GF}(C_2H_6) = 1.66 \pm 0.06$ and $\mathrm{GF(HCN)} = 1.68 \pm 0.07$, in contrast to $\mathrm{GF}(H_2O) = 2.53 \pm 0.10$; on UT December 18, $\mathrm{GF}(C_2H_6) = 1.60 \pm 0.04$ and $\mathrm{GF}(H_2O) = 2.59 \pm 0.08$ (Table 2).

We also expect that $Q_{nc}(H_2O)$ includes potential contributions from all sources of gas that may be important within the nucleus-centered FoV, which covers ±33 km in projected distance × 24 km in slit width. These sources include both direct nucleus sublimation and extended gas release in the innermost coma. If the second contribution is not negligible (for example, if icy grains or chunks start to sublimate within the nucleus-centered FoV), $\mathrm{GF}(C_2H_6) \times Q_{nc}(H_2O)$ would provide an upper limit of the total water production rate due to nucleus sublimation alone.

The ratio between this upper limit of the release of H_2O directly from the nucleus and the total measured H_2O production rate is ~0.65, as retrieved independently on each

observing date. This leads to a lower limit of the extended source contribution of ∼35%.

We emphasize that relative abundances (Section 4.4) are not expressed as ratios of nucleus-centered but rather of global production rates. Therefore, uncertainties in both Q_{nc} and GF are propagated to the overall uncertainty in Q (see, for example, Bonev 2005; DiSanti et al. 2016, 2018). However, the IR line intensities of NH_3 (UT December 17; Figure 4) are not sufficiently strong for spatial and Q-curve analysis. We therefore assumed that its (unconstrained) GF could be in the wide range between that of H_2O (GF = 2.53 ± 0.10) and HCN (GF = 1.68 ± 0.10, which is in excellent agreement with the GF values for the cosampled species C_2H_6 and C_2H_2). The uncertainty in $Q(NH_3)$ is then dominated by the assumed wide range in GF.

Only an upper limit is measured for formaldehyde (H_2CO), for which we adopt the larger GF for water. This is the more conservative choice because adopting the significantly smaller GF measured for other species would result in a more stringent upper limit.

In addition to the GF parameter, our production rates are sensitive to the assumed gas outflow speed (v_{gas}) of the parent species, which cannot be constrained directly from IR observations. We therefore adopt $v_{gas} = 0.8$ (km s^{-1}) $\times R_h^{-0.5} \approx 0.78$ km s^{-1}, in good agreement with the sunward hemisphere and the mean expansion speeds (∼0.8 and ∼0.7 km s^{-1}, respectively) measured through velocity-resolved ALMA (M. A. Cordiner et al. 2020, in preparation) and IRAM (N. Biver, private communication) observations. Assuming the lower outflow velocities reported by Coulson et al. (2020; ∼0.6 km s^{-1}) and Wang et al. (2020; ∼0.5 km s^{-1}) would decrease the overall production rates proportionally. However, unlike absolute production rates, the assumed outflow speed has a negligible effect on the relative abundance ratios, discussed in the next section.

4.4. Compositional Abundances Relative to H_2O and C_2H_6

Our measurements add to the still quite limited database of native species in JFCs and the overall chemical taxonomy of comets. For parent volatiles, this taxonomy has been built almost exclusively using H_2O as a "baseline" for expressing relative abundances (X/H_2O, where X is any volatile). This choice includes important information because abundances are expressed with respect to the principal volatile constituent of (most) comet nuclei (see Bockelée-Morvan et al. 2004; McKay et al. 2019). However, it is not exclusive, considering water may exhibit either similar or distinct outgassing sources (Section 4.1) and/or time-variability patterns in production rate compared to other species in a given comet. With this motivation, discussions at International Space Science Institute (ISSI-Bern) Team meetings[17] (2016–2018) suggested utilizing another easily detectable species, ethane, as a complementary compositional baseline (X/C_2H_6), in addition to X/H_2O.

Following this suggestion, Table 2 presents both X/H_2O and X/C_2H_6 abundance ratios in 46P/Wirtanen. NIRSPEC is optimal for such measurements because each spectrograph setting samples volatiles simultaneously with both H_2O and C_2H_6.

[17] ISSI-Bern Team No. 361 Project: "From Qualitative to Quantitative: Exploring the Early Solar System by Connecting Comet Composition and Protoplanetary Disk Models."

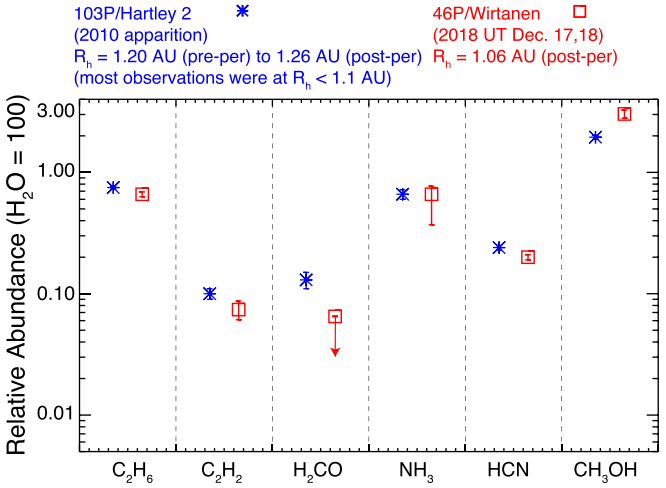

Figure 8. Comparison between volatile abundances ($H_2O = 100$) in 46P/Wirtanen (UT 2018 December 17–18) and EPOXI target 103P/Hartley 2. Comets 46P and 103P have colloquially been referred to as "twin" comets owing to their relatively high H_2O production rates for comets of similar size. For 103P, we show the mean values of measurements conducted during the 2010 apparition (Dello Russo et al. 2016), for which global coma abundance ratios did not vary significantly with time.

There is a tentative (at best) hint of a change in the relative abundance between our two baseline species ($C_2H_6/H_2O = 0.76 \pm 0.06$ and 0.66 ± 0.03, December 17 and 18, respectively; Table 2), mainly due to a ∼20% increase in the H_2O production rate on our second observing date. However, considering that even 1σ uncertainties in C_2H_6/H_2O nearly overlap, a definitive date-to-date variability cannot be claimed. For comparison, C_2H_6/H_2O has been found to vary among different comets by an order of magnitude (see Roth et al. 2018 and references within).

Figure 8 compares the composition of 46P/Wirtanen (X/H_2O) with that of EPOXI target 103P/Hartley 2 because 46P and 103P have colloquially been referred to as "twin" comets owing to their similar nucleus sizes and comparatively high (and similar) gas production rates. In terms of coma composition, 46P and 103P have quite similar abundances near perihelion for C_2H_6, C_2H_2, NH_3, and HCN. The most significant differences appear in the abundances of CH_3OH and especially native H_2CO (which is much lower in 46P/Wirtanen), with the CH_3OH/H_2CO abundance ratio in 46P closer to the highest measured values in comets, while 103P is in the more "typical" range (Dello Russo et al. 2016, 2020; Paganini et al. 2019).

5. Discussion

This section discusses our results and directions for future work in the context of coordinated observations of volatiles in 46P/Wirtanen (Section 5.1), fundamental questions on volatile outgassing (Sections 5.2–5.3), findings from the last two spacecraft missions to comets (Section 5.3), and further development of cometary compositional taxonomies (Section 5.4).

5.1. Synergistic Studies from NASA IRTF, ALMA, and JCMT

NASA IRTF. The 46P/Wirtanen campaign is an excellent example of the coordinated use of Keck and IRTF for comet science (Roth et al. 2021). While Keck offered unrivaled sensitivity on a 10 m telescope with the best spatial resolution

and longest slit (24″) available for near-IR studies, the IRTF provided temporal coverage in compositional measurements spanning over 2 months (see Dello Russo et al. 2019; Faggi et al. 2019a; Saki et al. 2020; Khan et al. 2021; McKay et al. 2021 for an overview and results from the IRTF campaign using the iSHELL spectrograph; see Protopapa et al. 2021 for using the SpeX instrument). Additional analyses are still in progress. When all results of the rich IRTF data set are finalized, a comparison between abundances and spatial associations measured at Keck and IRTF will be highly significant for understanding whether or not 46P/Wirtanen exhibits any temporal variability (hours to weeks) in outgassing patterns.

For a comet with an extended source of water observed very close to Earth, some of the H_2O might be released outside the narrow FoV of near-IR observations (both IRTF and Keck). This is a key consideration when IR-derived production rates are compared to those from other techniques sensitive to the more extended coma. The power law based on Solar and Heliospheric Observatory (SOHO) SWAN measurements ($Q = (1.90 \pm 0.16) \times 10^{28}\ R_h^{-8.6\pm0.7}$; postperihelion (Combi et al. 2020) implies a higher production rate (1.2×10^{28} s^{-1}) than our retrieval for December 17 and 18 (0.75 and 0.90×10^{28} s^{-1}, respectively). However, the 2018 SOHO postperihelion observations started after December 22; hence, they were not contemporaneous with our study. The H_2O production rate (0.77×10^{28} s^{-1}; Lis et al. 2019) based on a SOFIA/Great spectrum averaged over five dates (between December 14 and 22) is in good agreement with our December 17 value.

In addition, IRTF high-resolution spectra were taken with a significantly shorter slit (15″) than the data presented here (24″). Therefore, a comparison of X/H_2O abundances may include an evaluation of possible systematic differences due to different FoVs when measuring gas stemming from an extended source (Roth et al. 2021). Using a second compositional reference, for example, X/C_2H_6, as done in this work (see Section 4.4 and discussion in Section 5.4), will also be useful in searching for time variability in relative abundances.

ALMA and the James Clerk Maxwell Telescope (JCMT). Measurements at ALMA (Cordiner et al. 2019; M. A. Cordiner et al. 2020, in preparation) and Keck were 10 days apart, so a direct (i.e., excluding temporal variability) comparison is not possible for species covered by both techniques. With this major caveat, the very low abundance of (parent) H_2CO measured at Keck is very consistent with ALMA's 2D spatial map, which strongly suggests the release of H_2CO from a chemical precursor in the coma, mostly distributed outside the Keck FoV, hence our low reported abundance. In addition, early ALMA results imply that CH_3OH has both native (sublimation from the nucleus) and distributed (plausibly icy grain sublimation) sources, in agreement with the conclusion in this paper (Section 4.1). Finally, the CH_3OH gas rotational temperature distributions show T_{rot} rising from 80 K to ~100 K between zero and 150 km (sky-projected, azimuthally averaged distance from the nucleus) and then falling to ~50 K at 300 km; this implies one or more heating sources in the collisional coma working against near-adiabatic expansion cooling, as independently suggested from our IR measurements (Section 4.2).

Contemporaneous to Keck, observations with the JCMT (UT 2018 December 14–20) provide independently strong evidence for an extended source of CH_3OH and allow for the possibility that H_2CO is primarily a product species in 46P/Wirtanen (Coulson et al. 2020).

5.2. How Common Are Icy Grain Sources of Water in Comets?

The idea of icy grain "halos" dates back to (at least) early lab simulations of comet outgassing (Delsemme & Wenger 1970). EPOXI spacecraft imaging during the flyby of 103P/Hartley 2 demonstrated the possibility that in some comets, sublimating icy grains can be a considerable source of water gas (A'Hearn et al. 2011; Hermalyn et al. 2013; Kelley et al. 2013; Protopapa et al. 2014). Various remote-sensing techniques have provided independent evidence for significant icy grain sources of H_2O in some comets, including IR absorption from ices in the coma (C/2013 US10 Catalina; Protopapa et al. 2018), the dependence of H_2O production rate on aperture size (e.g., C/2009 P1 Garradd; Combi et al. 2013; Bodewits et al. 2014), and Sun–anti-Sun asymmetries (associated with nongravitational forces) in OH extended coma morphology (Knight & Schleicher 2013) or H_2O gas long-slit spatial profiles (e.g., Kawakita et al. 2013). This effect is most pronounced at favorable (closer to 90°) phase angles (for example, comet C/2007 W1 Boattini; Villanueva et al. 2011a), but might be noticeable even at the much smaller phase angle (~18°) of our observations (Figure 6).

In parallel, the development of DSMC coma thermodynamic models (Fougere 2014) showed that icy grain vaporization can be both a major contributor to the total H_2O production (up to ~80% in the split comet 73P-B/Schwassmann–Wachmann 3; Fougere et al. 2012) and a significant heating source for the inner collisional coma. Our spatially resolved measurements for H_2O column density and rotational temperature also support that vaporization from an extended source heats the coma and raises the overall water production of 46P, compared to outgassing solely from the nucleus (Sections 4.1–4.2).

All these findings address the following fundamental question: *how is water, the most abundant coma gas, released in comets*? The answer might vary from comet to comet, even when comets are compared only during their peak activity near perihelion. The increasing evidence for coma icy grain sources playing a major role in the overall gas production of some comets (103P, 73P-B, C/2007 W1, C/2009 P1, C/2013 US10, and plausibly 46P, but not 67P; see Section 1) reinforces specific questions for the prevalence (or lack thereof) of such sources among the broad comet population:

(1) How common and how important are coma icy grain sublimation sources of water?
(2) What factors determine whether water and other gases are being released directly from the nucleus, from an extended source, or through a combination of both?
(3) Do comets with comparatively high water production rates release a substantial fraction of their water through icy grain sublimation?
(4) If icy grain sources turn out to be common among many comets near perihelion, what is the primary activity driver that drags icy grains into the coma? In 103P/Hartley 2,

this was consistent with CO_2 sublimation directly from the nucleus.

Future near-IR and ALMA observations can help systematically address these questions through a combination of direct searches for icy grain spectral signatures (Protopapa et al. 2018) and spatially resolved measurements of coma temperatures and gas distributions, as reported in this work, because sublimation of coma grains is a major factor in inner coma thermodynamics. Furthermore, constraining the production rates and, when possible, spatial distributions of other species, such as CO_2 (detectable from space observatories, Ootsubo et al. 2012; McKay et al. 2016, 2019; and indirectly from the ground, McKay et al. 2013) is needed to evaluate their potential role in driving the overall activity in individual comets and in dragging water icy grains into the coma, as in 103P/Hartley 2.

5.3. Volatile Associations in 46P/Wirtanen versus EPOXI and Rosetta Findings

Both associations and differences in volatile release suggested by our spatial profiles (Section 4.1) bear some similarities with those found in spacecraft targets 103P/Hartley 2 (see references in Sections 4.1–4.2) and 67P/CG, including:

(1) Differences in outgassing patterns of H_2O and C_2H_6 in 46P, 103P, and 67P, with C_2H_6 being associated more closely with CO_2 (nucleus source) in both 103P and 67P.
(2) Distinct spatial morphologies of HCN and H_2O in 103P and 46P, which, similarly to C_2H_6, suggest different outgassing sources for the two volatiles or at least one additional (extended) outgassing source for H_2O. In 67P, where Rosetta studies had unprecedented coverage in R_h and revealed strong seasonal effects, HCN was sometimes closely associated with H_2O (Luspay-Kuti et al. 2015 pre-perihelion; $R_h \approx 3.34$ au) and at other times with CO_2 (Gasc et al. 2017; following equinox postperihelion, $R_h > \sim 2.8$ au).
(3) Similar spatial profiles for HCN and C_2H_6 in 46P and 103P. Interestingly, the C_2H_6/H_2O and HCN/H_2O relative abundances are correlated in a sample of ~30 comets (Dello Russo et al. 2016).
(4) Plausible association between HCN and C_2H_2 in both 46P and 103P.
(5) Extended sources of both H_2O and CH_3OH in 103P and 46P, in contrast to 67P, where outgassing from the nucleus strongly dominated (Biver et al. 2019), but could also be affected by redeposition of material between hemispheres (Gasc et al. 2017; Keller et al. 2017). Note that evaluating extended sources in 67P is still to be addressed in more detail as justified by Marschall et al. (2019) who tentatively postulate that sublimation from lifted dust/ice particles may be consistent with coma warming at ~40-50 km from the nucleus.

Similar findings in volatile release have also been suggested from additional ground-based studies, especially the detailed spatial measurements of comet C/2007 W1 Boattini (Villanueva et al. 2011a). An interesting direction for future work is then to test whether or not these patterns in outgassing are revealed in a larger sample of comets. As one example, we discuss water and methanol. Villanueva et al. (2011a) suggested that H_2O and CH_3OH might be stored together in the nucleus of C/2007 W1 in an ice component, which consists predominantly of polar species and which is distinct from the main source of apolar volatiles, like C_2H_6. Perhaps water and methanol can easily connect in an ice phase through O-H bonding, or comparatively lower volatility may also factor in their apparent link in some comets. Rosetta observed similar diurnal variations between H_2O and CH_3OH in 67P/CG (~3.34 pre-perihelion; Luspay-Kuti et al. 2015). Läuter et al. (2020) included CH_3OH in the "H_2O group of gases" based on the heliocentric power-law exponent in their "outbound" (postperihelion) production rates for $R_h = 2.4$–3.6 au. However, both this work and Biver et al. (2019) imply a more complex relationship between the sources of the two species, especially postperihelion. While nucleus sources dominated the release of water and methanol in 67P/CG, H_2O and CH_3OH have shown similar outgassing morphologies in comets like 103P and C/2007 W1, where these species likely have both nucleus and very significant extended sources. These findings motivate the questions: is there an association between H_2O and CH_3OH outgassing among the broad comet population, which is independent of the particular volatile release mechanism? Are there systematic differences in the release of H_2O and CH_3OH, compared to C_2H_6, C_2H_2, and HCN?

These questions can be emphasized in future Rosetta-type or flyby missions and further addressed by comparing spatial distributions in a larger number of comets observed from the ground, including 46P/Wirtanen on additional dates during the 2018 apparition, and also by testing whether the CH_3OH/H_2O relative abundance remains constant with time within ~2 au from the Sun. The spatial comparisons would be a stronger criterion, particularly for ground-based measurements. For example, the distinct associations in outgassing sources in 103P/Hartley 2 were revealed by the spacecraft flyby and by spatial distributions from ground-based studies, but not by the measured global (coma-averaged) relative abundances, which remained relatively constant during the course of several months when Hartley 2 was observed in 2010. This implied stability in the average (over all vaporization sources) volatile release (Mumma et al. 2011) but did not exclude heterogeneous outgassing, which is more directly testable through simultaneously measured spatial profiles.

Regardless of whether the hypothesis that, when observed in individual comets, the H_2O and CH_3OH association is independent of the volatile release mechanism, is rejected or validated, continued comparative spatial studies for these and other species would bring important insights about common trends (or lack thereof) in volatile outgassing among comets. This in turn would provide insight into how volatiles might be stored in the ices of comet nuclei. In the next section (see particularly Section 5.4.2), we suggest that such studies of spatial associations can and should be more closely integrated into the compositional taxonomy.

5.4. Extending the Compositional Taxonomy of Parent Volatiles

5.4.1. Ecliptic Comets: JFCs and 2P/Encke

The 2016–2019 period encompassed some of the very best apparitions of ecliptic comets in modern history. Because these short-period comets are often intrinsically fainter, they have been traditionally underrepresented in studies of all parent species (Dello Russo et al. 2014, 2016). Observations of 252P/LINEAR (Paganini et al. 2019), 45P/Honda–Mrkos–Pajdušáková (H-M-P; DiSanti et al. 2017; Dello Russo et al. 2020), 2P/Encke (Roth et al. 2018), 41P/Tuttle–Giacobini–Kresak (McKay et al. 2017), 21P/Giacobini–Zinner (Faggi et al. 2019b; Roth et al. 2020), and

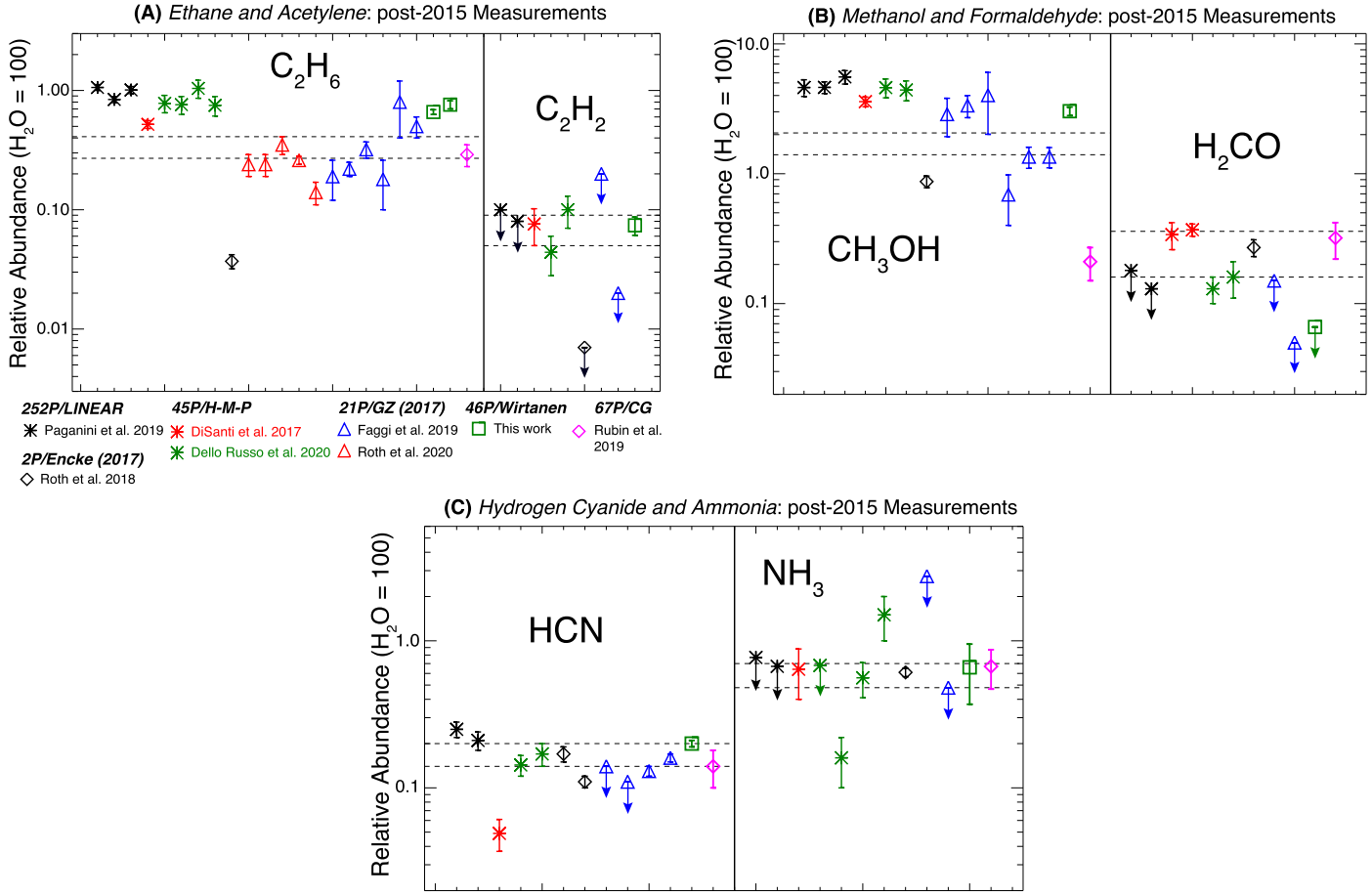

Figure 9. The 2016–2019 period encompassed some of the best apparitions of ecliptic comets in modern history, thereby improving our understanding of parent volatile composition for this dynamical class. Published abundances of (A) C_2H_6 and C_2H_2, (B) CH_3OH and (native) H_2CO, and (C) HCN and NH_3, from 2016–2019 near-IR studies are compared with our measurements in 46P/Wirtanen (green boxes) and with the bulk nuclear ice abundances deduced by the Rosetta/ROSINA team (pink diamonds; Rubin et al. 2019). The $\pm 1\sigma$ uncertainty intervals in mean abundances for comets observed prior to 2016 are indicated by dashed lines (taken from Dello Russo et al. 2016). In cases of nondetection of a particular species, two representative upper limits per study are shown.

46P/Wirtanen (this work; see also references in Section Section 5.1: Cordiner et al. 2019; Faggi et al. 2019a; Saki et al. 2020; and several ongoing analyses) have improved our understanding of the parent volatile release and ice content of ecliptic comets. Figures 9(A)–(C) show published abundances of C_2H_6, C_2H_2, CH_3OH, H_2CO, NH_3, and HCN, relative to water based on these more recent studies.

Figure 9 also shows the bulk nuclear ice abundances for 67P/CG deduced by the Rosetta team based on local coma measurements from the ROSINA mass spectrometer (Rubin et al. 2019). For C_2H_6, H_2CO, NH_3, and HCN, these bulk abundances fall very close to the current mean values for ecliptic comets. CH_3OH looks like an outlier, but only when compared to the small sample size of recently observed JFCs. Similar (or lower) CH_3OH abundance (<0.19%) has been constrained in comet C/1999 S4 LINEAR (Mumma et al. 2001; Lippi et al. 2020). Furthermore, Rosetta/MIRO observations (Biver et al. 2019) resulted in $CH_3OH/H_2O = 1.5\% \pm 0.1\%$, which falls within the range of previously observed JFCs.

5.4.2. The Value of Alternative Baselines for Compositional Measurements

Relative abundances of parent species have most commonly been expressed with respect to the dominant coma gas H_2O (Mumma et al. 2003; Bockelée-Morvan et al. 2004; DiSanti & Mumma 2008; Mumma & Charnley 2011; A'Hearn et al. 2012; Dello Russo et al. 2016; Rubin et al. 2019). The resulting X/H_2O abundance ratios vary among the studied comets. There is strong evidence that part of this variability reflects cosmogonic heritage (Dello Russo et al. 2007). However, the interpretation of comet-to-comet differences in X/H_2O is not straightforward.

First, differences in volatility are definitely expected to significantly affect coma abundances at larger heliocentric distances (e.g., Ootsubo et al. 2012). Second, even for comets observed at similar R_h (1–2 au), comet-to-comet variations may be a combined by-product of differences in natal conditions in the vast comet-forming regions (Willacy et al. 2015; Eistrup et al. 2019; and references therein) and perhaps of distinct postformative evolutionary histories (Bockelée-Morvan & Biver 2017; Keller & Kührt 2020). Third, seasonal and short-term temporal variability (or lack thereof) in both X/H_2O and any other coma relative abundance also needs to be better explored for parent volatiles in individual comets. Increasing the temporal coverage in the near-IR is gradually being addressed: from the more extended observing campaigns for several comets, including 46P/Wirtanen, to the first studies of parent species in JFCs during different perihelion passages (DiSanti et al. 2013; Roth et al. 2018, 2020; Faggi et al. 2019b).

In addition to increasing the temporal coverage, developing a chemical taxonomy based on alternative compositional baselines would likely provide a richer insight compared to using water alone. This approach has been fruitful in the taxonomy based on abundances of product species, where both OH and CN provided the most useful diagnostics (A'Hearn et al. 1995; Schleicher & Bair 2014, 2016; and references therein). We emphasize that the value of interpreting relative abundances among trace parent species has been well recognized in various works, for example, Villanueva et al. (2011a), Bonev et al. (2017), and McKay et al. (2019). Biver & Bockelée-Morvan (2019) used CH_3OH as an abundance reference for comparing measurements of complex organic molecules in comets, high- and low-mass protostars, and molecular clouds. Dello Russo et al. (2016) employed taxonomic classification in which abundances are related to both H_2O and HCN. This work showed that the abundance of C_2H_6 exhibits significantly smaller variability among comets, when expressed relative to HCN, compared to H_2O-based composition. Mumma et al. (2017, 2019) discussed the HCN/C_2H_6, NH_3/C_2H_6, HCN/H_2O, and C_2H_6/H_2O ratios in comets in order to explore the possibility that at least a fraction of cometary HCN might be a product species sourced in the innermost coma, and to provide evidence for the presence of ammoniated salts in comets. Lippi et al. (2020) presented insightful pie charts as a window to the abundance interrelationships among species other than H_2O.

For any trace species (X), in this paper, we report both X/H_2O and X/C_2H_6 abundances, as suggested during discussions within ISSI-Bern Team 361 (Section 4, Table 2). While not unique, ethane is a viable choice for an alternative baseline because:

(1) H_2O (polar molecule) and C_2H_6 (apolar molecule) tend to show distinct outgassing morphologies in 103P, 67P, and some comets studied only from the ground, including 46P (Figures 6(A) and (B)). This is a key point because a taxonomy based on alternative compositional baselines should also include a closer integration between global coma abundances and the underlying volatile associations in terms of common or distinct outgassing sources. If water and ethane tend to have notable differences in sources of volatile release, normalizing abundances to each of these species would provide a more in-depth view of the composition than using H_2O as the sole baseline.
(2) Unlike water, ethane is a "hypervolatile," with one of the lowest equilibrium sublimation temperatures among molecules covered in ground-based studies of comets.
(3) From a practical standpoint, in the near-IR, H_2O and C_2H_6 are comparatively easy to detect, so they have been measured in a larger number of comets, thereby making a taxonomic study with both baselines feasible.

To illustrate C_2H_6 as a complementary baseline, we compare comets 46P/Wirtanen and C/2007 W1 Boattini in X/H_2O (Figure 10(A)) and X/C_2H_6 (Figure 10(B)). Both comets revealed differing outgassing patterns for water and ethane and extended source(s) of H_2O, although the contribution of icy grain vaporization may be different in each comet. Abundances from the original study of C/2007 W1 by Villanueva et al. (2011a) were slightly modified by Lippi et al. (2020), which we compare with our 46P measurements.

Figure 10(A) shows X/H_2O ratios ($H_2O = 100$). In this representation, the two comets look different in CH_3OH, C_2H_6, and C_2H_2, which appear "enriched" in C/2007 W1 Boattini compared to 46P/Wirtanen.

Figure 10(B) shows X/C_2H_6 ratios ($C_2H_6 = 1$), which reveal a "complementary" picture: the two comets appear quite similar in the abundances of all measured species, except of course H_2O.

This example suggests that it is the differences between the X/H_2O and X/C_2H_6 comet classifications that might be most interesting. The X/H_2O measurements (Figure 10(A)) in C/2007 W1 might be affected by heterogeneous outgassing and extended H_2O release (including outside the FoV), while abundance ratios among trace species (Figure 10(B)) have been suggested as a better proxy of nucleus ice composition (Villanueva et al. 2011a).

We compared a nearly isotropic long-period comet, dynamically sourced in the Oort Cloud (C/2007 W1) with a short-period JFC linked to the scattered Kuiper disk (46P). Despite their vastly different dynamical histories, the two comets appear compositionally similar in X/C_2H_6 representation, consistent with the underlying volatile associations being primordial versus evolutionary.

We conclude this section by emphasizing one fundamental limitation in ethane-referenced abundance: as a symmetric hydrocarbon with no permanent dipole moment, C_2H_6 is observable only in the near-IR. Therefore, it will be of more limited use in interpreting studies at millimeter/submillimeter wavelengths, which are also very important for understanding the ice inventory preserved in comets. Coordinated contemporaneous near-IR and millimeter/submillimeter observations that provide C_2H_6 production rates could, to an extent, address this challenge. We hope, however, that the example of synergy between X/C_2H_6 and X/H_2O in compositional comparisons will stimulate further discussions on evolving the current cometary taxonomy for native species.

6. Summary

A major upgrade to the NIRSPEC instrument at the Keck II telescope was successfully completed in time for near-IR spectroscopic observations of comet 46P/Wirtanen during its historically close approach to Earth in 2018 December. The significant effort of the NIRSPEC team to complete the instrument upgrade on time for this investigation is greatly appreciated. The improvement in spectrograph sensitivity and especially in readout electronics is very pronounced with the new 2048×2048 HAWAII-2RG detector array.

These studies revealed abundances of several parent volatiles, including C_2H_2, C_2H_6, CH_3OH, NH_3, HCN, H_2CO, and H_2O. Together with long-slit spatial distributions for most of these species, the Keck observations resulted in one of the best data sets yet obtained for parent volatiles in ecliptic comets. Our main results are summarized as follows:

(1) The long-slit spatial distributions measured in 46P/Wirtanen are consistent with H_2O and very plausibly CH_3OH having an additional (more extended) source of gas release compared to HCN and C_2H_6. Because sublimation of H_2O from icy grains acts as a heating source in the inner (collisional) coma, these measurements are highly suitable for testing coma thermodynamic models.

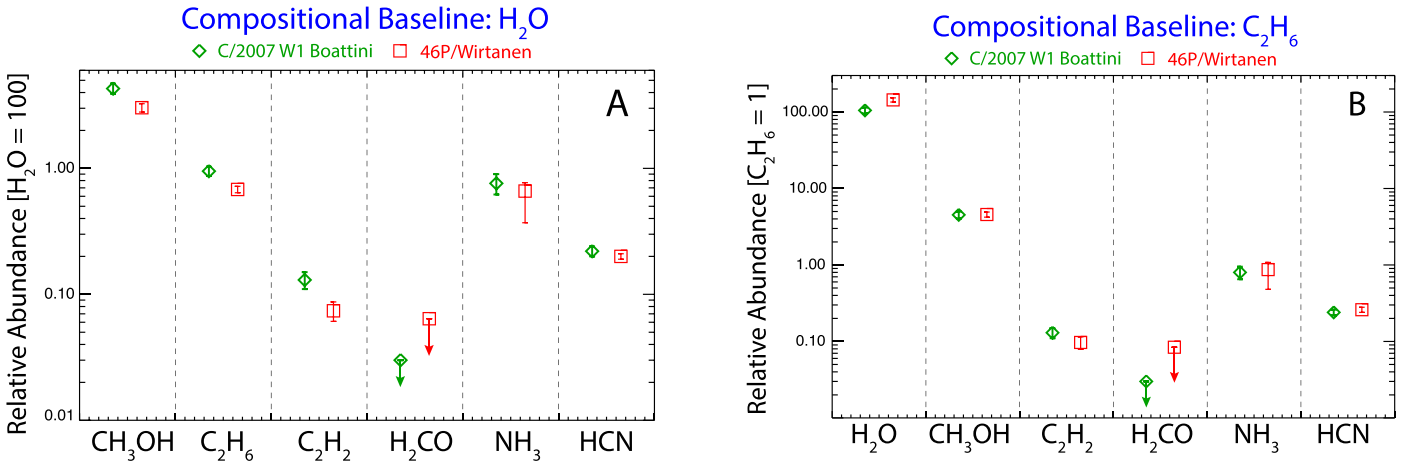

Figure 10. Comparison between the volatile composition of Oort Cloud comet C/2007 W1 Boattini (2007 July 9) and JFC 46P/Wirtanen (2018 December 17–18) using alternative compositional baselines (see Sections 4.4 and 5.4). (A) Using $H_2O = 100$ as the abundance reference. (B) Using $C_2H_6 = 1$ as the abundance reference.

(2) A rare opportunity to measure the spatial distribution of acetylene (C_2H_2) in a comet revealed that its outgassing is associated with the release of HCN and C_2H_6 in 46P/Wirtanen, rather than with H_2O.
(3) Associations in volatile release suggested by our spatial profiles bear some similarities to those found in spacecraft targets 103P/Hartley 2 and 67P/CG, as well as the Oort cloud comet C/2007 W1 Boattini studied from the ground. Placing high priority in comparative spatial studies in additional comets is expected to bring important insights into how volatiles are connected in the ices of comet nuclei. Such studies are needed to address whether or not C_2H_6, C_2H_2, and HCN have a common source of release (plausibly associated with CO_2) in a large number of comets, and whether or not systematic differences exist in the release of these species compared to H_2O and CH_3OH.
(4) The differences in spatial distributions are reflected in the measured relative abundances of species, which are then compared to those in other ecliptic comets. The deduced bulk abundances in JFC 67P/CG of C_2H_6, H_2CO, NH_3, and HCN relative to water from Rosetta/ROSINA (Rubin et al. 2019) fall well within the current range from ground-based observations of JFCs.
(5) Relative abundances in 46P/Wirtanen are reported using both H_2O and C_2H_6 as alternative abundance references. A chemical taxonomy extended to alternative compositional baselines should include closer integration between global coma abundances and the underlying volatile associations in terms of common or distinct outgassing sources. For example, if water and ethane tend to have notable differences in sources of volatile release among comets, a synergistic interpretation of X/C_2H_6 and X/H_2O classifications has strong potential to reveal deeper insights into comet composition than when utilizing each abundance reference alone.
(6) The choice of ethane is very useful, but definitely not exclusive. Extending the chemical taxonomy toward additional "baselines" for abundance measurements should also include species that can be more easily measured in a larger number of comets by both millimeter/submillimeter and near-IR methods, considering these are equally important windows to parent volatile composition. Species like CH_3OH and HCN are obvious candidates for compositional baselines across wavelength domains provided there are no systematic technique-dependent differences in measured production rates between IR and radio methods as possible for HCN. This volatile could be a key bridge between the compositional taxonomies of product and precursor species, provided it is established as the main source of CN. Continued spatially resolved studies of the release of CH_3OH, HCN, and C_2H_6 in an increasing sample of comets are both feasible and needed to further evaluate these species as complementary taxonomic baselines.

The 2018 apparition of 46P/Wirtanen was the best since its discovery, and also for years to come. This was a timely opportunity to study a JFC to a level of detail rarely affordable by ground-based studies. The resulting near-IR observations provided a transitional look between the very inner coma workings (as revealed by space missions) and the prevalent ground-based studies, which cover the more extended coma. We now have a much better picture of parent volatile abundances in 46P/Wirtanen and how they compare with other comets. These findings on both composition and volatile associations, along with coma environment with icy grains (and/or chunks), include information that would plausibly help future evaluations of 46P/Wirtanen as a prospective spacecraft target.

The authors wish to recognize and acknowledge the very significant cultural role and reverence that the summit of Maunakea has always had within the indigenous Hawaiian community. We are most fortunate and grateful to have the opportunity to conduct observations from this mountain.

This work would not be possible without the efforts of the entire team that completed the NIRSPEC upgrade. We thank the W. M. Keck Observatory for the support before and during these challenging observations. We thank Dr. Philip Muirhead for allowing us to be present during the post-upgrade NIRSPEC observation immediately preceding our study. We thank Dr. Tony Farnham, Dr. Kelly Fast, Dr. Nalin Samarasinha, and everyone involved in The Comet Wirtanen Observing Campaign for the excellent coordination of studies across wavelengths. We also thank Dr. Donna Pierce and Dr.

David Schleicher for constructive comments during the 2020 DPS/AAS virtual meeting, and Dr. Silvia Protopapa and Dr. Matthew Knight for valuable feedback.

This work was partly motivated by discussions at the International Space Science Institute in Bern during meetings of International Team 361, "*From Qualitative to Quantitative: Exploring the Early Solar System by Connecting Comet Composition and Protoplanetary Disk Models*."

This work was supported by a NASA Keck PI Data Award, administered by the NASA Exoplanet Science Institute. Data presented herein were obtained at the W. M. Keck Observatory from telescope time allocated to the National Aeronautics and Space Administration through the agency's scientific partnership with the California Institute of Technology and the University of California. The Observatory was made possible by the generous financial support of the W. M. Keck Foundation.

Various team members gratefully acknowledge NSF Astronomy and Astrophysics Postdoctoral Fellowship AST-1801978, NSF Astronomy and Astrophysics Research grants (AST-2009398, AST-2009910, AST-1616306, AST-1615441, and AST-1614471), the NASA Postdoctoral Program, and the NASA Earth and Space Science Fellowship (NNX16AP49H), Planetary Atmospheres (NNX14AG84G), Solar System Workings (NNX17AC86G, and 80NSSC20K0651), Solar System Observations (80NSSC17K0705, NNX17AI86G, and 18-SSO18_2-0040), and Emerging Worlds (80NSSC20K0341 and NNX15AH69G) programs. Support for collaborative observing programs HST-GO-15625 and HST-GO-15372 was provided by NASA through a grant from the Space Telescope Science Institute, which is operated by the Association of Universities for Research in Astronomy, Incorporated, under NASA contract NAS5-26555.

ORCID iDs

Boncho P. Bonev https://orcid.org/0000-0002-6391-4817
Neil Dello Russo https://orcid.org/0000-0002-8379-7304
Michael A. DiSanti https://orcid.org/0000-0001-8843-7511
Emily C. Martin https://orcid.org/0000-0002-0618-5128
Ronald J. Vervack, Jr. https://orcid.org/0000-0002-8227-9564
Geronimo L. Villanueva https://orcid.org/0000-0002-2662-5776
Hideyo Kawakita https://orcid.org/0000-0003-2011-9159
Erika L. Gibb https://orcid.org/0000-0003-0142-5265
Michael R. Combi https://orcid.org/0000-0002-9805-0078
Nathan X. Roth https://orcid.org/0000-0002-6006-9574
Mohammad Saki https://orcid.org/0000-0003-2277-6232
Adam J. McKay https://orcid.org/0000-0002-0622-2400
Martin A. Cordiner https://orcid.org/0000-0001-8233-2436
Dennis Bodewits https://orcid.org/0000-0002-2668-7248
Nicolas Biver https://orcid.org/0000-0003-2414-5370
Anita L. Cochran https://orcid.org/0000-0003-4828-7787
Younas Khan https://orcid.org/0000-0003-4773-2674
Kumar Venkataramani https://orcid.org/0000-0003-3321-1472

References

A'Hearn, M. F. 2017, RSPTA, 375, 20160261
A'Hearn, M. F., Belton, M. J. S., Delamere, W. A., et al. 2011, Sci, 6036, 1396
A'Hearn, M. F., Feaga, L. M., Keller, H. U., et al. 2012, ApJ, 758, 29
A'Hearn, M. F., Millis, R. C., Schleicher, D. O., Osip, D. J., & Birch, P. V. 1995, Icar, 118, 223
Biver, N., & Bockelée-Morvan, D. 2019, ACS Earth Space Chem., 3, 1550
Biver, N., Bockelée-Morvan, D., Hofstadter, M., et al. 2019, A&A, 630, A19
Bockelée-Morvan, D., & Biver, N. 2017, RSPTA, 375, 20160252
Bockelée-Morvan, D., Crovisier, J., Mumma, M. J., & Weaver, H. A. 2004, in Comets II, ed. M. C. Festou, H. U. Keller, & H. A. Weaver (Tucson: Univ. Arizona Press), 391
Bodewits, D., Farnham, T. L., A'Hearn, M. F., et al. 2014, ApJ, 786, 48
Bonev, B. P. 2005, PhD thesis, Univ. Toledo
Bonev, B. P., DiSanti, M. A., Villanueva, G. L., et al. 2014, ApJL, 796, L6
Bonev, B. P., Mumma, M. J., DiSanti, M. A., et al. 2006, ApJ, 653, 774
Bonev, B. P., Mumma, M. J., Kawakita, H., Kobayashi, H., & Villanueva, G. L. 2008, Icar, 196, 241
Bonev, B. P., Villanueva, G. L., DiSanti, M. A., et al. 2017, AJ, 153, 241
Bonev, B. P., Villanueva, G. L., Paganini, L., et al. 2013, Icar, 222, 740
Cochran, A. L., Levasseur-Regourd, A.-C., Cordiner, M., et al. 2015, SSRv, 197, 9
Combi, M. R., Cochran, A. L., Cochran, W. D., Lambert, D. L., & Johns-Krull, C. M. 1999, ApJ, 512, 961
Combi, M. R., Harris, W. M., & Smyth, W. H. 2004, in Comets II, ed. M. C. Festou, H. U. Keller, & H. A. Weaver (Tucson: Univ. Arizona Press), 523
Combi, M. R., Mäkinen, T., Bertaux, J.-L., et al. 2020, PSJ, 1, 72
Combi, M. R., Mäkinen, J. T. T., & Bertaux, J.-L. 2013, Icar, 225, 740
Combi, M. R., & Smyth, W. H. 1988, ApJ, 327, 1044
Cordiner, M. A., Biver, N., Crovisier, J., et al. 2017, ApJ, 837, 177
Cordiner, M. A., Biver, N., Milam, S. M., et al. 2019, in EPSC-DPS Joint Meeting 2019, 1131
Cordiner, M. A., Remijan, A. J., Boissier, J., et al. 2014, ApJL, 792, L2
Coulson, I. M., Liu, F.-Ch., Cordiner, M. A., et al. 2020, AJ, 160, 182
Cravens, T. E., & Körösmezey, A. 1986, P&SS, 34, 961
Crovisier, J., Biver, N., Bockelée-Morvan, D., et al. 2009, EM&P, 105, 267
Dello Russo, N., DiSanti, M. A., Mumma, M. J., Magee-Sauer, K., & Rettig, T. W. 1998, Icar, 135, 377
Dello Russo, N., Kawakita, H., Bonev, B., et al. 2020, Icar, 335, 113411
Dello Russo, N., Kawakita, H., Vervack, R. J., & Weaver, H. A. 2016, Icar, 278, 301
Dello Russo, N., McKay, A. J., Saki, M., et al. 2019, in EPSC-DPS Joint Meeting 2019, 742
Dello Russo, N., Mumma, M. J., DiSanti, M. A., et al. 2006, Icar, 184, 255
Dello Russo, N., Vervack, R. J., Kawakita, H., et al. 2014, Icar, 238, 125
Dello Russo, N., Vervack, R. J., Lisse, C. M., et al. 2011, ApJL, 734, L8
Dello Russo, N., Vervack, R. J., Weaver, H. A., et al. 2007, Natur, 448, 172
Dello Russo, N., Vervack, R. J., Weaver, H. A., et al. 2013, Icar, 222, 707
Delsemme, A. H., & Wenger, A. 1970, P&SS, 18, 709
DiSanti, M. A., Bonev, B. P., Dello Russo, N., et al. 2017, AJ, 154, 246
DiSanti, M. A., Bonev, B. P., Gibb, E. L., et al. 2016, ApJ, 820, 34
DiSanti, M. A., Bonev, B. P., Gibb, E. L., et al. 2018, AJ, 156, 258
DiSanti, M. A., Bonev, B. P., Magee-Sauer, K., et al. 2006, ApJ, 650, 470
DiSanti, M. A., Bonev, B. P., Villanueva, G. L., & Mumma, M. J. 2013, ApJ, 763, 1
DiSanti, M. A., & Mumma, M. J. 2008, SSRv, 138, 127
DiSanti, M. A., Mumma, M. J., Dello Russo, N., & Magee-Sauer, K. 2001, Icar, 153, 361
DiSanti, M. A., Mumma, M. J., Geballe, T. R., & Davies, J. K. 1995, Icar, 116, 1
DiSanti, M. A., Villanueva, G. L., Paganini, L., et al. 2014, Icar, 228, 167
Drozdovskaya, M. N., Walsh, C., van Dishoeck, E. F., et al. 2016, MNRAS, 462, 977
Eistrup, C., Walsh, C., & van Dishoeck, E. F. 2019, A&A, 629, A84
Faggi, S., Mumma, M. J., Villanueva, G. L., Paganini, L., & Lippi, M. 2019a, in EPSC-DPS Joint Meeting 2019, 1018
Faggi, S., Mumma, M. J., Villanueva, G. L., Paganini, L., & Lippi, M. 2019b, AJ, 158, 254
Farnham, T. L., Knight, M., Schleicher, D. G., et al. 2021, PSJ, 2, 7
Fink, U. 2009, Icar, 201, 311
Fougere, N. 2014, PhD thesis, Univ. Michigan
Fougere, N., Altwegg, K., Berthelier, J.-J., et al. 2016, A&A, 588, A134
Fougere, N., Combi, M. R., Rubin, M., & Tenishev, V. 2013, Icar, 225, 688
Fougere, N., Combi, M. R., Tenishev, V., et al. 2012, Icar, 221, 174
Gasc, S., Altwegg, K., Balsiger, H., et al. 2017, MNRAS, 469, S108
Gombosi, T. I., Nagy, A. F., & Cravens, T. E. 1986, RvGeo, 24, 667
Groussin, O., & Lamy, P. 2003, A&A, 412, 879
Hermalyn, B., Farnham, T. L., Collins, S. M., et al. 2013, Icar, 222, 625
Jehin, E., Manfroid, J., Pozuelos, 1, et al. 2018, CBET, 4585, 1

Kamp, I. 2020, in IAU Proc. 345, Origins: From the Protosun to the First Steps of Life (Cambridge: Cambridge Univ. Press), 115
Kawakita, H., Kobayashi, H., Dello Russo, N., et al. 2013, Icar, 222, 723
Keller, H. U., & Kührt, E. 2020, SSRv, 216, 14
Keller, H. U., Mottola, S., Hviid, S. F., et al. 2017, MNRAS, 469, S357
Kelley, M. S., Farnham, T. L., Li, J.-Y., et al. 2021, PSJ, submitted
Kelley, M. S., Lindler, D. J., Bodewits, D., et al. 2013, Icar, 222, 634
Khan, Y., Gibb, E. L., Bonev, B. P., et al. 2021, PSJ, 2, 20
Knight, M. M., & Schleicher, D. G. 2013, Icar, 222, 691
Knight, M., Schleicher, D. G., Farnham, T. L., et al. 2021, PSJ, submitted
Läuter, M., Kramer, T., Rubin, M., & Altwegg, K. 2020, MNRAS, 498, 3995
Lippi, M., Villanueva, G. L., Mumma, M. J., et al. 2020, AJ, 159, 157
Lis, D. C., Bockelée-Morvan, D., Güsten, R., et al. 2019, A&A, 625, L5
Luspay-Kuti, A., Hässig, M., Fuselier, S. A., et al. 2015, A&A, 583, A4
Marschall, R., Rezac, L., Kappel, D., et al. 2019, Icar, 328, 104
Martin, E. C., Fitzgerald, M. P., McLean, I. S., et al. 2018, Proc. SPIE, 10702, 107020A
Martin, E. C., Fitzgerald, M. P., McLean, I. S., Kress, E., & Wang, E. 2016, Proc. SPIE, 9908, 99082R
McKay, A., DiSanti, M. A., Cochran, A. L., et al. 2017, AAS/DPS Meeting, 49, 305.09
McKay, A. J., Chanover, N. J., Morgenthaler, J. P., et al. 2013, Icar, 222, 684
McLean, I. S., Becklin, E. E., Bendiksen, O., et al. 1998, Proc. SPIE, 3354, 566
McKay, A. J., DiSanti, M. A., Kelley, M. S. P., et al. 2019, AJ, 158, 128
McKay, A. J., Kelley, M. S. P., Cochran, A. L., et al. 2016, Icar, 266, 249
McKay, A. J., DiSanti, M. A., Cochran, A. L., et al. 2021, PSJ, 2, 21
Moulane, Y., Jehin, E., José Pozuelos, F., et al. 2019, EPSC-DPS Joint Meeting 2019, 13, 1036
Mumma, M. J., Bonev, B. P., Villanueva, G. L., et al. 2011, ApJL, 734, L7
Mumma, M. J., & Charnley, S. B. 2011, ARA&A, 49, 471
Mumma, M. J., Charnley, S. B., & Cordiner, M. A. 2019, EPSC-DPS Joint Meeting 2019, 13, 1916
Mumma, M. J., Charnley, S. B., Cordiner, M., Paganini, L., & Villanueva, G. L. 2017, AAS/DPS Meeting, 49, 414.19
Mumma, M. J., Dello Russo, N., DiSanti, M. A., et al. 2001, Sci, 292, 1334
Mumma, M. J., DiSanti, M. A., Dello Russo, N., et al. 2003, AdSpR, 31, 2563
Ootsubo, T., Kawakita, H., Hamada, S., et al. 2012, ApJ, 752, 15
Paganini, L., Camarca, M. N., Mumma, M. J., et al. 2019, AJ, 158, 98
Paganini, L., DiSanti, M. A., Mumma, M. J., et al. 2014a, AJ, 147, 15
Paganini, L., Mumma, M. J., Villanueva, G. L., et al. 2014b, ApJ, 791, 122
Protopapa, S., Kelley, M. S. P., Woodward, C. E., & Yang, B. 2021, PSJ, submitted
Protopapa, S., Kelley, M. S. P., Yang, B., et al. 2018, ApJL, 862, L16
Protopapa, S., Sunshine, J. M., Feaga, L. M., et al. 2014, Icar, 238, 191
Radeva, Y. L., Mumma, M. J., Villanueva, G. L., & A'Hearn, M. F. 2011, ApJ, 729, 135
Roth, N. X., Gibb, E. L., Bonev, B. P., et al. 2018, AJ, 156, 251
Roth, N. X., Gibb, E. L., Bonev, B. P., et al. 2020, AJ, 159, 42
Roth, N. X., Milam, S. N., Cordiner, M. A., et al. 2021, PSJ, in press
Rubin, M., Altwegg, K., Balsiger, H., et al. 2019, MNRAS, 489, 594
Saki, M., Gibb, E. L., Bonev, B. P., et al. 2020, AJ, 160, 184
Schleicher, D., & Bair, A. 2014, in Proc. of Conf. on Asteroids, Comets, Meteors, ed. K. Muinonen (Helsinki) 475
Schleicher, D., & Bair, A. 2016, AAS/DPS Meeting, 48, 308.04
Shou, Y., Combi, M., Toth, G., et al. 2016, ApJ, 833, 160
Tenishev, V., Combi, M. R., & Davidsson, B. 2008, ApJ, 685, 659
Tenishev, V., Combi, M. R., & Rubin, M. 2011, ApJ, 732, 104
Villanueva, G. L., DiSanti, M. A., Mumma, M. J., & Xu, L.-H. 2012a, ApJ, 747, 37
Villanueva, G. L., Mumma, M. J., Bonev, B. P., et al. 2009, ApJL, 690, L5
Villanueva, G. L., Mumma, M. J., Bonev, B. P., et al. 2012b, JQSRT, 113, 202
Villanueva, G. L., Mumma, M. J., DiSanti, M. A., et al. 2011a, Icar, 216, 227
Villanueva, G. L., Mumma, M. J., & Magee-Sauer, K. 2011b, JGRE, 116, E08012
Villanueva, G. L., Smith, M. D., Protopapa, S., Faggi, S., & Mandell, A. M. 2018, JQSRT, 217, 86
Wang, Z., Zhang, S.-B., Tseng, W.-L., et al. 2020, AJ, 159, 240
Willacy, K., Alexander, C., Ali-Dib, M., et al. 2015, SSRv, 197, 151
Xie, X., & Mumma, M. J. 1992, ApJ, 386, 720
Xie, X., & Mumma, M. J. 1996, ApJ, 464, 457
Zakharov, V. V., Rodionov, A. V., Lukyanov, G. A., & Crifo, J. F. 2008, Icar, 194, 327